Journal of Computational Physics 229 (2010) 6874–6897

Contents lists available at ScienceDirect

Journal of Computational Physics

journal homepage: www.elsevier.com/locate/jcp

Nonuniform time-step Runge–Kutta discontinuous Galerkin method for Computational Aeroacoustics

Li Liu [a], Xiaodong Li [a,*], Fang Q. Hu [b]

[a] School of Jet Propulsion, Beihang University, Beijing 100191, People's Republic of China
[b] Department of Mathematics and Statistics, Old Dominion University, Norfolk, VA 23529, United States

ARTICLE INFO

Article history:
Received 10 April 2009
Received in revised form 10 May 2010
Accepted 21 May 2010
Available online 8 June 2010

Keywords:
Runge–Kutta method
Discontinuous Galerkin method
Nonuniform time-step size
Computational Aeroacoustics

ABSTRACT

With many superior features, Runge–Kutta discontinuous Galerkin method (RKDG), which adopts Discontinuous Galerkin method (DG) for space discretization and Runge–Kutta method (RK) for time integration, has been an attractive alternative to the finite difference based high-order Computational Aeroacoustics (CAA) approaches. However, when it comes to complex physical problems, especially the ones involving irregular geometries, the time step size of an explicit RK scheme is limited by the smallest grid size in the computational domain, demanding a high computational cost for obtaining time accurate numerical solutions in CAA. For computational efficiency, high-order RK method with nonuniform time step sizes on nonuniform meshes is developed in this paper. In order to ensure correct communication of solutions on the interfaces of grids with different time step sizes, the values at intermediate-stages of the Runge–Kutta time integration on the elements neighboring such interfaces are coupled with minimal dissipation and dispersion errors. Based upon the general form of an explicit p-stage RK scheme, a linear coupling procedure is proposed, with details on the coefficient matrices and execution steps at common time-levels and intermediate time-levels. Applications of the coupling procedures to Runge–Kutta schemes frequently used in simulation of fluid flow and acoustics are given, including the third-order TVD scheme, and low-storage low dissipation and low dispersion (LDDRK) schemes. In addition, an analysis on the stability of coupling procedures on a nonuniform grid is carried out. For validation, numerical experiments on one-dimensional and two-dimensional problems are presented to illustrate the stability and accuracy of proposed nonuniform time-step RKDG scheme, as well as the computational benefits it brings. Application to a one-dimensional nonlinear problem is also investigated.

1. Introduction

With many superior features, Runge–Kutta discontinuous Galerkin (RKDG) method, which adopts discontinuous Galerkin approximation in space and explicit Runge–Kutta integration in time, has been widely applied in modeling advection-dominant physical phenomena [34,6,7,20,21,1,33]. For aeroacoustic calculations, in order to simulate the acoustic waves propagating from near field to far field, a long time integration with low dissipation and low dispersion errors is usually required in a large space domain. In this regard, a variety of high-order Runge–Kutta methods have been applied, for instance, the classical third and fourth order methods [25], the third-order TVD methods [18], and the optimized schemes with minimized dispersion and dissipation errors [22,4,2]. Typically they are designed for a uniform time step size in the entire computational domain [3]. However, when it comes to realistic complex problems, especially the ones involving irregular

* Corresponding author. Tel.: +86 10 82338579; fax: +86 10 82316108.
E-mail address: lixd@buaa.edu.cn (X. Li).

0021-9991/$ - see front matter © 2010 Elsevier Inc. All rights reserved.
doi:10.1016/j.jcp.2010.05.028

geometries and the ones involving a large disparity of physical scales, nonuniform grids are usually adopted for modeling resolution requirement and simulation effectiveness. For such cases, the time step size would be limited by the smallest grid size due to stability requirements for explicit Runge–Kutta schemes. Consequently, with a uniform time step for the entire computational domain, excessive computational time would be required for obtaining time-dependant numerical solutions, which results in a barrier for many practical applications. Clearly, due to the popularity of Runge–Kutta schemes, there is a need for the extension of Runge–Kutta methods to nonuniform time steps.

Over the past few decades, many efforts have been made to achieve time marching with variable time step sizes. Multirate time integration schemes for both multi-step (Adam–Bashforth) methods and multi-stage (Runge–Kutta) methods for ordinary differential equations have been actively developed [16,19,35]. The interpolation and the extrapolation on time are the most direct approaches to realize multirate time stepping strategy [35,30], which are suitable for arbitrary ratio of time step size. An early work on local time stepping for discontinuous Galerkin schemes is given in [12]. A recent application of the multi-step method with local time stepping to the discontinuous Galerkin method can be found in [17]. In [38,13], Adam–Bashforth type multi-step time integration schemes with nonuniform time step sizes are optimized in Cartesian and curvilinear grid in conjunction with multiple grid size dispersion relation preserving (DRP) finite difference schemes. Local time stepping methods based on the Cauchy–Kovalevskaja (CK) procedures, which are sometimes called the Lax–Wendroff procedures, have also been developed rapidly, with arbitrary ratio of time-step sizes and be of arbitrary high order accuracy in the framework of the ADER schemes (arbitrary high order schemes using derivatives) [11], such as the ADER finite volume (ADER-FV) [10,39], and the ADER discontinuous Galerkin (ADER-DG) [32,8,9] and the ADER finite difference (ADER-FD) schemes, and the space–time expansion DG scheme (STE-DG) [14,15]. We also mention a recent effort in [28] on using the additive Runge–Kutta schemes for overcoming the time step restrictions imposed by a few small-sized elements.

In the present work, explicit Runge–Kutta method with nonuniform time step (NUTS RK) on nonuniform meshes is considered, where the spatial discretization is carried out by the discontinuous Galerkin (DG) method. For correct communication of solutions between meshes with different time step sizes, the coupling of values at intermediate stages of Runge–Kutta time integration should be implemented synchronously for the elements neighboring the interfaces with low dissipation and low dispersion errors. Formulation of the coupling procedures for multi-stage Runge–Kutta integration will be presented based on the linearity of the equation. It makes the time marching with local time step available for the Runge–Kutta family of time integration schemes, and is valid for an arbitrary time step ratio. Without any interpolation or extrapolation algorithm, the coupling procedures maintain the same high order accuracy as that of the RK scheme for linear problems and second order accurate for nonlinear problems. Numerical validations in one- and two-dimensional cases are performed to demonstrate the stability, accuracy of the scheme for both linear and nonlinear cases, as well as the computational benefits in those cases.

The remainder of the paper is organized as follows: discontinuous Galerkin spatial discretization is reviewed in Section 2. In Section 3, the linear coupling procedure that is capable of handling nonuniform time-step integration on a nonuniform grid is formulated based upon the general form of an explicit p-stage Runge–Kutta scheme, and an optimization of coupling coefficients with low dissipation and low dispersion errors is discussed. A stability analysis for the nonuniform time-step RKDG scheme is given in Section 4. Finally, the numerical experiments are conducted to validate the method in one- and two-dimensional problems in Section 5. Section 6 gives the conclusions.

2. The discontinuous Galerkin spatial discretization

For convenience of discussion, we first briefly review a DG semi-discretization for partial differential equations (PDE). Consider a system of hyperbolic PDE of the form given below in a domain $\Omega \subset \mathbb{R}^d$:

$$\frac{\partial \mathbf{U}}{\partial t} + \nabla \cdot \mathbf{F} = \mathbf{S}, \tag{1}$$

where the solution $\mathbf{U} : \Omega \times [0,T] \mapsto \mathbb{R}^n$ ($n \geqslant d$) is an n-vector valued function, and the flux $\mathbf{F}$ is given by $\mathbf{F} = \mathbf{F}(\mathbf{U},\mathbf{x},t)$ while the source term by $\mathbf{S} = \mathbf{S}(\mathbf{U},\mathbf{x},t)$. Here, d is the number of space dimensions. For linear problems, the flux $\mathbf{F}$ can be written as $\mathbf{F} = \mathbf{A}\mathbf{U}$, and $\mathbf{A}$ is a vector with Jacobian matrices as entries, $\mathbf{A} = (A_1,\ldots,A_d)$ and $\nabla = \left(\frac{\partial}{\partial x_1},\ldots,\frac{\partial}{\partial x_d}\right)$.

In the DG method, the computational domain of interest Ω is divided into non-overlapping elements,

$$\Omega = \bigcup_{k=1}^{N_e} \Omega_k$$

and the approximation space V_h is continuous within each element, but could be discontinuous across element interfaces. The space V_h is obtained by defining on each element Ω_k the local polynomial space $\mathcal{P}(\Omega_k)$ which contains only spatial functions in the semi-discrete formulation

$$V_h = \{v \in L^1(\Omega) : v|\Omega_k \in \mathcal{P}(\Omega_k)\}. \tag{2}$$

Let the local basis set in Ω_k be $\mathcal{B}_k = \{v_\ell^k\}_{\ell=1,\ldots,N}$, which is usually chosen to be the same for all elements; and N is the degree of freedom in Ω_k that is dependent on the number of space dimensions d and the order of scheme P. Then the local approximate solution $\mathbf{U}_h$ in Ω_k can be expressed in an expansion of the local basis set $\mathcal{B}_k$ as

$$\mathbf{U}_h|_{\Omega_k}(\mathbf{x},t)=\sum_{\ell=1}^{N}\mathbf{C}_\ell^k(t)\,v_\ell^k(\mathbf{x}), \tag{3}$$

where $\mathbf{C}_\ell^k$ are the expansion coefficients of the solution in $\mathcal{B}_k$. It has been shown that the accuracy of the method can reach $P+1/2$ on the general triangular grid, and even $P+1$ on some Cartesian grid and some semi-uniform triangular grid when the order of polynomial space is P [29,26,27,31].

By an integration by parts, the weak formulation of DG spatial discretization in Ω_k can be obtained as

$$\int_{\Omega_k} v_{\ell'}\frac{\partial \mathbf{U}_h^k}{\partial t}\,\mathrm{d}\mathbf{x}+\int_{\partial\Omega_k} v_{\ell'}\mathbf{F}^R\cdot\mathbf{n}\,\mathrm{d}\mathbf{s}-\int_{\Omega_k}\mathbf{F}\frac{\partial v_{\ell'}}{\partial x}\,\mathrm{d}\mathbf{x}=\int_{\Omega_k} v_{\ell'}\mathbf{S}\,\mathrm{d}\mathbf{x}, \tag{4}$$

where $\partial\Omega_k$ is the boundary of Ω_k, and $v_{\ell'}$ are test functions which are assumed to be the same as the basis polynomials in the Galerkin method. $\mathbf{F}^R$ is the numerical flux at element boundary. Since the discontinuities are permitted at the interfaces of elements in the DG method, some numerical flux approximation should be adopted. Various numerical formulas for flux approximation have been proposed in the literature (see, e.g. [23,33], and the references cited therein). Most of the approximations can be generalized as

$$\mathbf{F}^R=\mathbf{H}(\mathbf{U}_L,\mathbf{U}_R,\mathbf{n}), \tag{5}$$

where $\mathbf{U}_L$ and $\mathbf{U}_R$ are the approximation values of $\mathbf{U}$ on the left and the right side of the element edge, which is directed by the orientation of the normal vector of the edge pointing outside of the dominant element, $\mathbf{n}$, according to the right-hand rule. For linear problems, the numerical flux can be expressed as

$$\mathbf{F}^R=\overline{\mathbf{A}}_L\mathbf{U}_L+\overline{\mathbf{A}}_R\mathbf{U}_R. \tag{6}$$

Let $\overline{\mathbf{A}}=\sum_{i=1}^{d}A_i n_i$. Then for the characteristics-based flux

$$\overline{\mathbf{A}}_L=\frac{\overline{\mathbf{A}}+\theta|\overline{\mathbf{A}}|}{2},\quad \overline{\mathbf{A}}_R=\frac{\overline{\mathbf{A}}-\theta|\overline{\mathbf{A}}|}{2}$$

and for the Lax–Friedrich flux

$$\overline{\mathbf{A}}_L=\frac{\overline{\mathbf{A}}+\theta\lambda_{max}\mathbf{I}}{2},\quad \overline{\mathbf{A}}_R=\frac{\overline{\mathbf{A}}-\theta\lambda_{max}\mathbf{I}}{2},$$

where λ_{max} is the absolute maximum of the eigenvalues of $\overline{\mathbf{A}}$, and θ is an upwind-parameter that is usually chosen to be a positive real number between 0 and 1.

Introducing a proper local coordinate given by $\boldsymbol{\xi}=\{\xi_i\}_{i=1,\ldots,d}$, the volume integration in Eq. (4) can be evaluated conveniently in the reference element $\widehat{\Omega}_k$ using the Jacobian $\mathbf{J}_k$, while the surface integral term is still computed in physical domain. Then the weak integral equation for time integration can be obtained as

$$\mathbf{Q}\frac{\partial \mathbf{C}^k}{\partial t}+\frac{1}{J_k}\int_{\partial\Omega_k} v_{\ell'}\mathbf{F}^R\,\mathrm{d}\mathbf{s}-\int_{\widehat{\Omega}_k}\nabla v_{\ell'}\mathbf{J}_k^{-1}\mathbf{F}\,\mathrm{d}\boldsymbol{\xi}=\int_{\widehat{\Omega}_k} v_{\ell'}\mathbf{S}\,\mathrm{d}\boldsymbol{\xi} \tag{7}$$

where $\mathbf{Q}$ is mass matrix, and

$$\mathbf{J}_k\equiv\frac{\partial(x_1,\ldots,x_d)}{\partial(\xi_1,\ldots,\xi_d)},\quad J_k=|\mathbf{J}_k|.$$

In what follows, we will discuss an extension of Runge–Kutta method to the solution of semi-discrete equation with nonuniform time-step sizes. However, the developed method is not only valid for discontinuous Galerkin method but also, with proper modifications, applicable to other spatial discretization methods, such as the finite difference schemes.

3. Nonuniform time-step Runge–Kutta method

High-order explicit Runge–Kutta schemes are frequently used for time integration in aeroacoustic computations, for example, the classical Runge–Kutta schemes [5], the third-order TVD Runge–Kutta scheme [18], and the optimized low dissipation and low dispersion Runge–Kutta (LDDRK) schemes [22,36]. Most of these schemes are developed with a uniform time step size. For computational efficiency, linear coupling procedures for high-order Runge–Kutta time integration scheme with nonuniform time-step size will be developed in this section.

3.1. Linear formulation

After a spatial discretization, such as the DG scheme discussed in the previous section, the semi-discrete equations for time integration can be modeled as

$$\frac{\partial \mathbf{U}}{\partial t} = F(\mathbf{U}), \tag{8}$$

where $\mathbf{U}$ represents the unknown vector. The general explicit p-stage Runge–Kutta time integration scheme with step Δt can be written as

$$\begin{aligned}
&\mathbf{k}_1 = F(\mathbf{U}^n),\\
&\mathbf{k}_2 = F(\mathbf{U}^n + \Delta t a_{21}\mathbf{k}_1),\\
&\cdots\cdots\\
&\mathbf{k}_p = F(\mathbf{U}^n + \Delta t[a_{p1}\mathbf{k}_1 + a_{p2}\mathbf{k}_2 + \cdots + a_{pp-1}\mathbf{k}_{p-1}]),\\
&\mathbf{U}^{n+1} = \mathbf{U}^n + \Delta t\sum_{i=1}^{p} b_i\mathbf{k}_i,
\end{aligned} \tag{9}$$

where $\mathbf{U}^n$ and $\mathbf{U}^{n+1}$ indicate the numerical solutions at time level t_n and $t_{n+1} = t_n + \Delta t$, respectively. Here, $\mathbf{k}_i$ is the ith stage value within one Runge–Kutta step. For convenience of discussion, $\mathbf{U}$ will be considered as a scalar function in the formulation hereafter. The extension to the vector case is straightforward.

We first consider a case of nonuniform grid as illustrated in Fig. 1, which serves as a schematic of the interface between coarse and fine meshes. The coarse mesh time-step Δt_c is twice of the fine mesh time-step Δt_f, i.e.

$$\Delta t_c = 2\Delta t_f. \tag{10}$$

Although a ratio of 1/2 could be a common choice at grid interfaces, efficiency considerations on grid partitioning may lead to a larger or smaller ratio. As we will see, the basic formulation presented below can be extended to case with an arbitrary ratio of time-step sizes.

Under assumption (10), the coarse mesh solution will advance one step while the fine mesh solution would advance two steps. As shown in Fig. 1, we will refer to the level $t_{n+1} = t_n + \Delta t_c = t_n + 2\Delta t_f$ as the *common time level*, where the solutions on both fine and coarse meshes would step forward synchronously; and time level $t_{n+1/2} = t_n + \Delta t_f$ as the *intermediate time level*, where only the solution on fine mesh would be integrated. The interval $[t_n, t_{n+1}]$ forms a time slab in the multirate time integration. The time stepping within a time slab is assumed to be constant. Specifically, within a typical time slab $[t_n, t_{n+1}]$, the solution on the coarse mesh is advanced forward one step to $t_{n+1} = t_n + \Delta t_c$ by the integration formulas

$$\begin{aligned}
&\mathbf{k}_{c,1} = F(\mathbf{U}_c^n),\\
&\mathbf{k}_{c,2} = F(\mathbf{U}_c^n + \Delta t_c a_{21}\mathbf{k}_{c,1}),\\
&\cdots\cdots\\
&\mathbf{k}_{c,p} = F(\mathbf{U}_c^n + \Delta t_c[a_{p1}\mathbf{k}_{c,1} + a_{p2}\mathbf{k}_{c,2} + \cdots + a_{pp-1}\mathbf{k}_{c,p-1}]),\\
&\mathbf{U}_c^{n+1} = \mathbf{U}_c^n + \Delta t_c\sum_{i=1}^{p} b_i\mathbf{k}_{c,i},
\end{aligned} \tag{11}$$

Synchronously, for the solution on the fine mesh, the first time-step in the Runge–Kutta integration with step Δt_f from t_n to $t_{n+1/2} = t_n + \Delta t_f$ is

$$\begin{aligned}
&\mathbf{k}_{f,1}^{(1)} = F\left(\mathbf{U}_f^n\right)\\
&\mathbf{k}_{f,2}^{(1)} = F\left(\mathbf{U}_f^n + \Delta t_f a_{21}\mathbf{k}_{f,1}^{(1)}\right)\\
&\cdots\cdots\\
&\mathbf{k}_{f,p}^{(1)} = F\left(\mathbf{U}_f^n + \Delta t_f\left[a_{p1}\mathbf{k}_{f,1}^{(1)} + a_{p2}\mathbf{k}_{f,2}^{(1)} + \cdots + a_{pp-1}\mathbf{k}_{f,p-1}^{(1)}\right]\right),\\
&\mathbf{U}_f^{n+\frac{1}{2}} = \mathbf{U}_f^n + \Delta t_f\sum_{i=1}^{p} b_i\mathbf{k}_{f,i}^{(1)}.
\end{aligned} \tag{12}$$

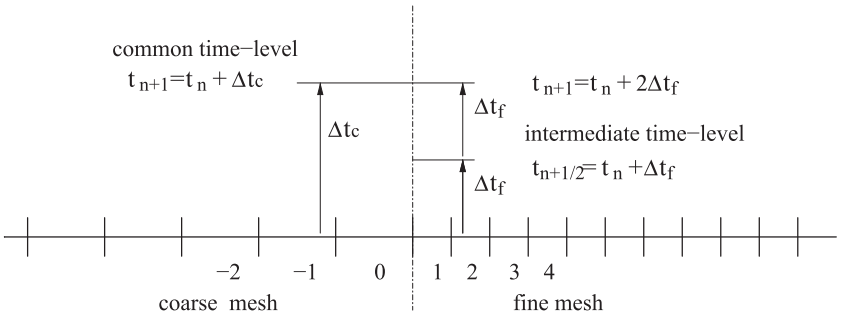

Fig. 1. Sketch of a nonuniform mesh with nonuniform time-step.

At intermediate time level, the second step in fine mesh $t_{n+1/2}$ to $t_{n+1} = t_n + 2\Delta t_f$ is carried out as

$$\begin{aligned}
&\mathbf{k}_{f,1}^{(2)} = F\left(\mathbf{U}_f^{n+\frac{1}{2}}\right),\\
&\mathbf{k}_{f,2}^{(2)} = F\left(\mathbf{U}_f^{n+\frac{1}{2}} + \Delta t_f a_{21}\mathbf{k}_{f,1}^{(2)}\right),\\
&\cdots\cdots\\
&\mathbf{k}_{f,p}^{(2)} = F\left(\mathbf{U}_f^{n+\frac{1}{2}} + \Delta t_f [a_{p1}\mathbf{k}_{f,1}^{(2)} + a_{p2}\mathbf{k}_{f,2}^{(2)} + \cdots + a_{pp-1}\mathbf{k}_{f,p-1}^{(2)}]\right),\\
&\mathbf{U}_f^{n+1} = \mathbf{U}_f^{n+\frac{1}{2}} + \Delta t_f \sum_{i=1}^{p} b_i \mathbf{k}_{f,i}^{(2)}.
\end{aligned} \tag{13}$$

In the above, subscripts 'c' and 'f' have been used to denote the solutions in the coarse and fine meshes, respectively.

Since the numerical flux approximation is applied at the interface of neighboring elements, the spatial operator $F(\mathbf{U})$ appeared on the right-hand side of Eqs. (11)–(13) is dependent on values in adjacent elements. Consequently, for elements next to an interface of fine and coarse meshes, the stage values on the coarse mesh are needed for spatial discretization operator on the fine mesh, and vice versa. A suitable coupling procedure should be employed to ensure correct communication of the neighboring elements with different time step sizes.

The relations that are necessary to implement a nonuniform time-step Runge–Kutta scheme described above can be summarized as follows, in which we will use an over tilde to denote the coupling values computed in a coarse/fine element that are to be used in the time integration of a neighboring fine/coarse element:

1. For the synchronous stepping in the coarse and the fine mesh at the start of a time slab:
   - (1.a) Vector $\{\tilde{\mathbf{k}}_{f,i}\}_{i=1,2,\ldots,p}$ should be computed from known $\{\mathbf{k}_{f,i}^{(1)}\}_{i=1,2,\ldots,p}$ in fine mesh for use in time advancing in coarse mesh in (11).
   - (1.b) Vector $\{\tilde{\mathbf{k}}_{c,i}^{(1)}\}_{i=1,2,\ldots,p}$ should be computed from known $\{\mathbf{k}_{c,i}\}_{i=1,2,\ldots,p}$ in coarse mesh for use in time advancing in fine mesh in (12).
2. For time stepping in the fine mesh at intermediate time-level:
   - (2.a) Vector $\{\tilde{\mathbf{k}}_{c,i}^{(2)}\}_{i=1,2,\ldots,p}$ should be computed from known $\{\mathbf{k}_{c,i}\}_{i=1,2,\ldots,p}$ in coarse mesh for use in time advancing in fine mesh at the intermediate time level in (13).

For linear problems, relations (1.a), (1.b) and (2.a) can be established by the fact that stage values $\{\mathbf{k}_i\}$ in the Runge–Kutta scheme are directly related to the time derivatives of $\mathbf{U}$. An analysis of Runge–Kutta scheme (9) shows that

$$\begin{bmatrix}\mathbf{k}_1\\ \mathbf{k}_2\\ \cdot\\ \cdot\\ \cdot\\ \mathbf{k}_p\end{bmatrix} = \underbrace{\begin{bmatrix}1 & 0 & 0 & \cdot & \cdot & 0\\ 1 & c_{22} & 0 & \cdot & \cdot & 0\\ 1 & c_{32} & c_{33} & \cdot & \cdot & 0\\ \cdot & \cdot & \cdot & \cdot & \cdot & \cdot\\ \cdot & \cdot & \cdot & \cdot & \cdot & \cdot\\ 1 & c_{p2} & c_{p3} & \cdot & \cdot & c_{pp}\end{bmatrix}}_{\mathbf{C}} \underbrace{\begin{bmatrix}1 & 0 & 0 & \cdot & \cdot & 0\\ 0 & \Delta t & 0 & \cdot & \cdot & 0\\ 0 & 0 & \Delta t^2 & \cdot & \cdot & \cdot\\ \cdot & \cdot & \cdot & \cdot & \cdot & \cdot\\ \cdot & \cdot & \cdot & \cdot & \cdot & \cdot\\ 0 & 0 & 0 & \cdot & \cdot & \Delta t^{p-1}\end{bmatrix}}_{\mathbf{P}_{\Delta t}} \begin{bmatrix}\frac{\partial \mathbf{U}}{\partial t}\\ \frac{\partial^2 \mathbf{U}}{\partial t^2}\\ \cdot\\ \cdot\\ \cdot\\ \frac{\partial^p \mathbf{U}}{\partial t^p}\end{bmatrix}_{t=t_n}, \tag{14}$$

where c_{ij} are related to the Runge–Kutta coefficients a_{ij} by

$$\begin{aligned}
&c_{22} = a_{21},\\
&c_{32} = a_{31} + a_{32}, \qquad c_{33} = a_{32}a_{21},\\
&c_{42} = a_{41} + a_{42} + a_{43}, \qquad c_{43} = a_{43}a_{32} + a_{43}a_{31} + a_{42}a_{21},\\
&c_{44} = a_{43}a_{32}a_{21},\\
&\cdots\cdots\\
&c_{p,2} = a_{p,1} + \cdots + a_{p,p-1}, \qquad c_{p,3} = a_{p,p-1}a_{p-1,p-2} + \cdots + a_{p,2}a_{21},\\
&\cdots\\
&c_{p,p} = a_{p,p-1}a_{p-1,p-2}\cdots a_{21} \quad (a_{p,p-1}a_{p-1,p-2}\cdots a_{21} \neq 0).
\end{aligned} \tag{15}$$

Under the assumption $a_{p,p-1}a_{p-1,p-2}\cdots a_{21} \neq 0$, which is true for the majority of Runge–Kutta family, by (14) it is straightforward to get the relation between $\{\tilde{\mathbf{k}}_{f,i}\}$ and $\{\mathbf{k}_{f,i}^{(1)}\}$ in the fine elements neighboring the interface as

$$\begin{bmatrix} \tilde{\mathbf{k}}_{f,1} \\ \tilde{\mathbf{k}}_{f,2} \\ \cdot \\ \cdot \\ \cdot \\ \tilde{\mathbf{k}}_{f,p} \end{bmatrix} = \mathbf{C}\mathbf{P}_{\Delta t_c}\mathbf{P}_{\Delta t_f}^{-1}\mathbf{C}^{-1} \begin{bmatrix} \mathbf{k}_{f,1}^{(1)} \\ \mathbf{k}_{f,2}^{(1)} \\ \cdot \\ \cdot \\ \cdot \\ \mathbf{k}_{f,p}^{(1)} \end{bmatrix} \equiv \mathbf{T}_f \begin{bmatrix} \mathbf{k}_{f,1}^{(1)} \\ \mathbf{k}_{f,2}^{(1)} \\ \cdot \\ \cdot \\ \cdot \\ \mathbf{k}_{f,p}^{(1)} \end{bmatrix} \tag{16}$$

and similarly, the relation between $\{\tilde{\mathbf{k}}_{c,i}^{(2)}\}$ and $\{\mathbf{k}_{c,i}\}$ in the coarse elements neighboring the interface is

$$\begin{bmatrix} \tilde{\mathbf{k}}_{c,1}^{(1)} \\ \tilde{\mathbf{k}}_{c,2}^{(1)} \\ \cdot \\ \cdot \\ \cdot \\ \tilde{\mathbf{k}}_{c,p}^{(1)} \end{bmatrix} = \mathbf{C}\mathbf{P}_{\Delta t_f}\mathbf{P}_{\Delta t_c}^{-1}\mathbf{C}^{-1} \begin{bmatrix} \mathbf{k}_{c,1} \\ \mathbf{k}_{c,2} \\ \cdot \\ \cdot \\ \cdot \\ \mathbf{k}_{c,p} \end{bmatrix} \equiv \mathbf{T}_c^{(1)} \begin{bmatrix} \mathbf{k}_{c,1} \\ \mathbf{k}_{c,2} \\ \cdot \\ \cdot \\ \cdot \\ \mathbf{k}_{c,p} \end{bmatrix}. \tag{17}$$

Obviously, the coupling matrix $\mathbf{T}_c^{(1)}$ is the inverse of $\mathbf{T}_f$. These are the relations for (1.a) and (1.b) for linear problems. It is important to note that they are both lower-triangular matrices. Consequently, the coupling procedures can be carried out synchronously in both coarse and fine meshes on every stage at the start of a time slab.

Further, relations for (2.a) can be established by utilizing a Taylor series expansion of (9) at the intermediate time level. For linear cases, the Taylor series expansion of $\{\mathbf{k}_{c,i}\}$ at $t_{n+1/2} = t_n + \Delta t_f$ up to order p will be used. Specifically, we have

$$\begin{bmatrix} \mathbf{k}_1 \\ \mathbf{k}_2 \\ \cdot \\ \cdot \\ \cdot \\ \mathbf{k}_p \end{bmatrix}_{t=t_n+\Delta t_f} \approx \mathbf{C}\mathbf{P}_{\Delta t_f}\mathbf{B}_{\Delta t_f} \begin{bmatrix} \frac{\partial \mathbf{U}}{\partial t} \\ \frac{\partial^2 \mathbf{U}}{\partial t^2} \\ \cdot \\ \cdot \\ \cdot \\ \frac{\partial^p \mathbf{U}}{\partial t^p} \end{bmatrix}_{t=t_n}, \tag{18}$$

where $\mathbf{B}_{\Delta t_f}$ is an upper-triangular matrix of the form

$$\mathbf{B}_{\Delta t_f} = \begin{bmatrix} 1 & b_{12}\Delta t_f & b_{13}\Delta t_f^2 & \cdot & \cdot & b_{1p}\Delta t_f^{p-1} \\ 0 & 1 & b_{23}\Delta t_f & \cdot & \cdot & b_{2p}\Delta t_f^{p-2} \\ 0 & 0 & 1 & \cdot & \cdot & b_{3p}\Delta t_f^{p-3} \\ \cdot & \cdot & \cdot & \cdot & \cdot & \cdot \\ \cdot & \cdot & \cdot & \cdot & \cdot & \cdot \\ 0 & 0 & 0 & \cdot & \cdot & 1 \end{bmatrix} \tag{19}$$

When no optimization is applied, b_{ij} are just the coefficients of Taylor series expansion given below:

$$b_{ij} = \frac{1}{(j-i)!}$$

Using (14) and (18), $\{\tilde{\mathbf{k}}_{c,i}^{(2)}\}$ that is needed in the second step of the fine mesh can be calculated from the known $\{\mathbf{k}_{c,i}\}$ by the following equation:

$$\begin{bmatrix} \tilde{\mathbf{k}}_{c,1}^{(2)} \\ \tilde{\mathbf{k}}_{c,2}^{(2)} \\ \cdot \\ \cdot \\ \cdot \\ \tilde{\mathbf{k}}_{c,p}^{(2)} \end{bmatrix} = \mathbf{C}\mathbf{P}_{\Delta t_f}\mathbf{B}_{\Delta t_f}\mathbf{P}_{\Delta t_c}^{-1}\mathbf{C}^{-1} \begin{bmatrix} \mathbf{k}_{c,1} \\ \mathbf{k}_{c,2} \\ \cdot \\ \cdot \\ \cdot \\ \mathbf{k}_{c,p} \end{bmatrix} \equiv \mathbf{T}_c^{(2)} \begin{bmatrix} \mathbf{k}_{c,1} \\ \mathbf{k}_{c,2} \\ \cdot \\ \cdot \\ \cdot \\ \mathbf{k}_{c,p} \end{bmatrix} \tag{20}$$

which establishes the relation (2.a).

With the formulas for the coupling matrices $\mathbf{T}_f$, and $\mathbf{T}_c^{(s)}$, $s = 1, 2$, given above, the coupling procedures can be carried out as described in (11)–(13).

The formulation introduced above is derived for a general explicit p-stage Runge–Kutta scheme. It can be applied readily to specific Runge–Kutta schemes. The difference in the extensions for different RK schemes lies only on coefficient matrix $\mathbf{C}$

in formula (14). In this sense, the formulation presented here is general for linear problems. More details on the extension to the schemes frequently used in CAA are given in Appendix.

What need to be pointed out is that for linear problems, the algorithm is of the same order of accuracy as that of the Runge–Kutta scheme for time integration. However, for nonlinear problems, because the truncation error in formula (14) is reduced to be $\mathcal{O}(\Delta t^2)$, the accuracy of the algorithm is of second order.

3.2. Application to arbitrary ratio of time-step size

In practice, considerations of grid partitioning and computational efficiency may result in a ratio of time-step sizes other than 1/2. The formulation presented above can be extended to a more general time-step ratio.

We first generalize the coupling formulas described in the previous subsection for a mesh interface between time step Δt_1 and Δt_2 of arbitrary ratio, as shown in Fig. 2. To advance a time step Δt_1 in mesh 1 from t_n to $t_n + \Delta t_1$, the Runge–Kutta stage values on mesh 2 at time t_n is needed. Following the analysis in 3.1, the necessary Runge–Kutta stage values in mesh 2 to be used for mesh 1 can be readily obtained as

$$[\widetilde{\mathbf{K}}_2]_{t=t_n} = \mathbf{C}\mathbf{P}_{\Delta t_1}\mathbf{B}_{\Delta\tau_2}\mathbf{P}_{\Delta t_2}^{-1}\mathbf{C}^{-1}[\mathbf{K}_2]_{t=t_{m-1}}, \tag{21}$$

where $[\widetilde{\mathbf{K}}_2]$ denotes the resultant column vector of the necessary stage values in mesh 2 for use in mesh 1 at time level t_n, computed from the known stage values at the nearest earlier time level t_{m-1} in the neighboring mesh of Δt_2. Matrix $\mathbf{B}_{\Delta\tau_2}$ has the same definition as (19) and here

$$\Delta\tau_2 = t_n - t_{m-1}. \tag{22}$$

Similarly, to advance a time step Δt_2 in mesh 2 from t_m to $t_m + \Delta t_2$, the necessary RK stage values in mesh 1 to be used in mesh 2 is

$$[\widetilde{\mathbf{K}}_1]_{t=t_m} = \mathbf{C}\mathbf{P}_{\Delta t_2}\mathbf{B}_{\Delta\tau_1}\mathbf{P}_{\Delta t_1}^{-1}\mathbf{C}^{-1}[\mathbf{K}_1]_{t=t_n}, \tag{23}$$

where

$$\Delta\tau_1 = t_m - t_n. \tag{24}$$

At the start of a time slab where $\Delta\tau = 0$, matrix $\mathbf{B}_{\Delta\tau}$ becomes the identity matrix, and (21) and (23) will be consistent with (16) and (17) in 3.1. Thus, the formulas (21) and (23) are a generalization of the coupling procedures both at the start of time slabs and the time stepping within time slabs.

Using (21) and (23), the time integrations for grid points with different time steps of an arbitrary ratio can be carried out synchronously. As an example, the coupling procedures for time step ratio 2/3 will be described in detail. The grid structure and time levels for a time slab $[t_n, t_{n+1}]$ are illustrated in Fig. 3 where

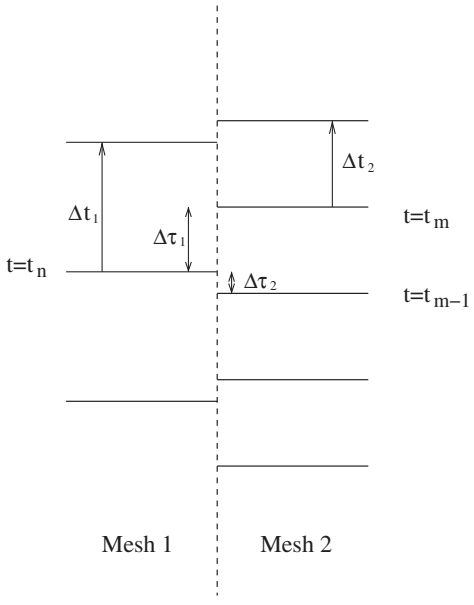

Fig. 2. Schematics of an interface between meshes of Δt_1 and Δt_2.

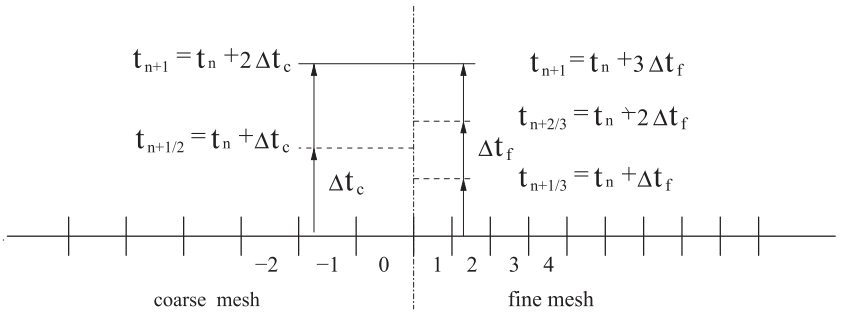

Fig. 3. A nonuniform mesh with nonuniform time-step Δt_c:Δt_f = 3:2.

$$\Delta t_c = \frac{3}{2}\Delta t_f. \tag{25}$$

Let $[\mathbf{K}_c^{(s)}],\ s = 1,2$ and $[\mathbf{K}_f^{(s)}],\ s = 1,2,3$ be stage value vectors at the sth time level within the time slab for the coarse and the fine mesh respectively, and $[\widetilde{\mathbf{K}}_f^{(s)}],\ s = 1,2$ and $[\widetilde{\mathbf{K}}_c^{(s)}],\ s = 1,2,3$ be the vectors for coupling procedures. The necessary relations for implementation of a nonuniform time-step Runge–Kutta scheme shown in Fig. 3 can be summarized as follows:

1. For the synchronous step in the coarse mesh and the first step in the fine mesh:
   (1.a) Vector $[\widetilde{\mathbf{K}}_f^{(1)}]$ should be computed from known $[\mathbf{K}_f^{(1)}]$ in fine mesh for the time advancing in coarse mesh;
   (1.b) Vector $[\widetilde{\mathbf{K}}_c^{(1)}]$ should be computed from known $[\mathbf{K}_c^{(1)}]$ in coarse mesh for the time advancing in fine mesh.
2. For the second step in the fine mesh:
   (2.a) Vector $[\widetilde{\mathbf{K}}_c^{(2)}]$ should be computed from known $[\mathbf{K}_c^{(1)}]$ in coarse mesh for the time advancing in fine mesh.
3. For the second step in the coarse mesh:
   (3.a) Vector $[\widetilde{\mathbf{K}}_f^{(2)}]$ should be computed from known $[\mathbf{K}_f^{(2)}]$ in fine mesh for the time advancing in coarse mesh.
4. For the third step in the fine mesh:
   (4.a) Vector $[\widetilde{\mathbf{K}}_c^{(3)}]$ should be computed from known $[\mathbf{K}_c^{(2)}]$ in coarse mesh for the time advancing in fine mesh.

These relations can be realized by formulas given in (21) and (23). Specifically, we have

For (1.a):

$$[\widetilde{\mathbf{K}}_f^{(1)}] = \mathbf{C}\mathbf{P}_{\Delta t_c}\mathbf{P}_{\Delta t_f}^{-1}\mathbf{C}^{-1}[\mathbf{K}_f^{(1)}] \equiv \mathbf{T}_f^{(1)}[\mathbf{K}_f^{(1)}]. \tag{26}$$

For (1.b):

$$[\widetilde{\mathbf{K}}_c^{(1)}] = \mathbf{C}\mathbf{P}_{\Delta t_f}\mathbf{P}_{\Delta t_c}^{-1}\mathbf{C}^{-1}[\mathbf{K}_c^{(1)}] \equiv \mathbf{T}_c^{(1)}[\mathbf{K}_c^{(1)}]. \tag{27}$$

For (2.a):

$$[\widetilde{\mathbf{K}}_c^{(2)}] = \mathbf{C}\mathbf{P}_{\Delta t_f}\mathbf{B}_{\Delta t_f}\mathbf{P}_{\Delta t_c}^{-1}\mathbf{C}^{-1}[\mathbf{K}_c^{(1)}] \equiv \mathbf{T}_c^{(2)}[\mathbf{K}_c^{(1)}]. \tag{28}$$

For (3.a):

$$[\widetilde{\mathbf{K}}_f^{(2)}] = \mathbf{C}\mathbf{P}_{\Delta t_c}\mathbf{B}_{\frac{1}{2}\Delta t_f}\mathbf{P}_{\Delta t_f}^{-1}\mathbf{C}^{-1}[\mathbf{K}_f^{(2)}] \equiv \mathbf{T}_f^{(2)}[\mathbf{K}_f^{(2)}]. \tag{29}$$

For (4.a):

$$[\widetilde{\mathbf{K}}_c^{(3)}] = \mathbf{C}\mathbf{P}_{\Delta t_f}\mathbf{B}_{\frac{1}{2}\Delta t_f}\mathbf{P}_{\Delta t_c}^{-1}\mathbf{C}^{-1}[\mathbf{K}_c^{(2)}] \equiv \mathbf{T}_c^{(3)}[\mathbf{K}_c^{(2)}]. \tag{30}$$

In practice, the coupling matrices can be stored and do not need to be computed at each time step. Moreover, the coupling is only carried out for elements next to the interfaces of nonuniform time steps, so the additional storage and computational time incurred due to coupling are limited.

3.3. Optimization with minimal dissipation and dispersion errors

Runge–Kutta schemes with low dissipation and low dispersion errors are preferred in CAA. In order to minimize the dissipation and dispersion errors in the coupling procedures presented previously, we study a possible optimization of the coefficient matrices at intermediate levels. The coefficients in the first row in formula (19), $\{b_{1j}\}_{j=2,3,\ldots,p}$ will be modified so that the numerical amplification factor at intermediate time level will be consistent with that of corresponding LDDRK scheme [22], which is already optimized to have the minimal dissipation and dispersion errors.

Table 1
Optimized coefficients for LDDRK schemes at different time levels.

Stages	Level	b_{14}	b_{15}	b_{16}
4	2	0.1629970000	–	–
	3	0.1657492500	–	–
	4	0.1662589258	–	–
5	2	0.1665580000	0.03944976670	–
	3	0.1666304445	0.04126266474	–
	4	0.1666545926	0.04157650988	–
6	2	1/3!	0.04166666670	0.007810050010
	3	1/3!	0.04166666669	0.008300628140
	4	1/3!	0.04166666670	0.008326873060

Note. The 1st level is the start of the time slab; $b_{12} = 1$, $b_{13} = 1/2$.

The case with integral time-step size ratio m:1 is considered here for convenience, for which the coupling procedures are only carried out on the coarse mesh.

Consider the model equation $\partial u/\partial t = -q\partial u/\partial x$. Upon Fourier expansion, the numerical amplification factor of Runge–Kutta integration with time step Δt_f can be expressed in the form of

$$r_o = 1 + \sum_{j=1}^{p} c_j(-\mathbf{i}\sigma)^j, \tag{31}$$

where $\sigma = qk^*\Delta t_f$, and k^* is only dependent on spatial discretization; for LDDRK schemes c_j are the coefficients given in [22]. After m steps advancing with uniform step size, the factor should be r_o^m.

After applying coupling procedure, the amplification factor at an intermediate time level in coarse mesh becomes

$$\tilde{r} = 1 + \sum_{j=1}^{p} \gamma_j(-\mathbf{i}\sigma)^j, \tag{32}$$

where σ has the same definition as before, and coefficients $\{\gamma_j\}_{j=1,2,\ldots,p}$ are related to $\{b_{1j}\}_{j=2,3,\ldots,p}$ by formula (18) and (19).

Thus the amplification factors of nonuniform time-step advancing with ratio m:1 can be obtained within a time slab by

$$\begin{aligned} \tilde{r}_c^{(1)} &= r_o, \\ \tilde{r}_c^{(k)} &= \tilde{r}_c^{(k-1)}\tilde{r} \\ &= \left(1 + \sum_{j=1}^{p} c_j(-\mathbf{i}\sigma)^j\right)^{k-1}\left(1 + \sum_{j=1}^{p} \gamma_j(-\mathbf{i}\sigma)^j\right), \quad k = 2, 3, \ldots, m, \end{aligned} \tag{33}$$

where $\tilde{r}_c^{(k)}$ is the factor of the coupling procedure at the kth intermediate time level, of which the first one at the start of the time slab is r_o. By comparing the factor $\tilde{r}_c^{(k)}$ with that of LDDRK integration, r_o^k, a linear system for b_{1j} is yielded.

The optimized coefficients turn out to be practically the same for all intermediate time-levels (second level, third level, ...) within one coarse time step of different integral time-step ratios. Table 1 shows the optimized coefficients for $m = 2, 3, 4$. Once the optimized coefficients $\{b_{1j}\}_{j=2,3,\ldots,p}$ have been determined, the matrices $\mathbf{B}$ and $\mathbf{T}_c^{(2)}$ are to be found by formulas (19) and (20). The extension to the cases with arbitrary time-step size ratios is straightforward. In actual computation, however, since the coupling procedure affects only a few elements next to the interfaces of nonuniform meshes, the benefit of this optimization to the solution on the whole domain has been found to be moderate.

4. Stability analysis

In this section, we consider the stability of the coupling procedure proposed in previous sections. Specifically, we study the stability of computation for a nonuniform mesh shown in Fig. 4 when the nonuniform Runge–Kutta scheme is applied to the one-dimensional wave equation

$$\frac{\partial u}{\partial t} + q\frac{\partial u}{\partial x} = 0, \quad x \in \Omega, \ \ t \leqslant \mathbf{T}, \tag{34}$$

where u is the unknown, and q is the speed of the wave. We also assume periodic boundary condition in our stability analysis.

In Fig. 4, the total number of elements is assumed to be $2N_e$, with N_e elements, indexed from 1 to N_e, in the fine mesh region and N_e elements, indexed from $-N_e + 1$ to 0, in the coarse mesh region. For interior elements, the semi-discrete DG approximation can be written as

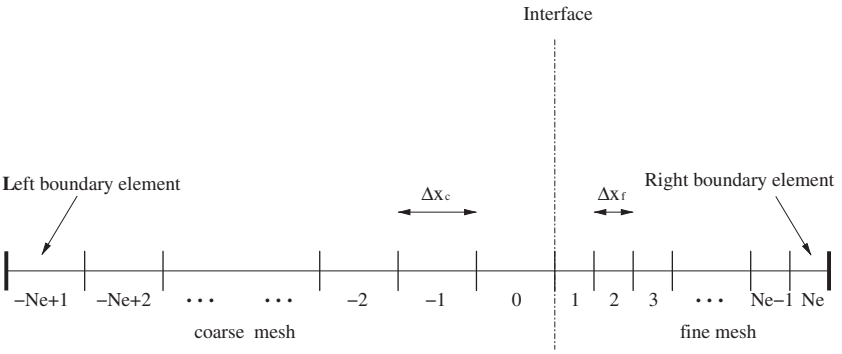

Fig. 4. Schematic of a finite nonuniform mesh composed of two blocks.

$$\frac{d\mathbf{C}^k}{dt} = \frac{1}{\Delta x_k}[\mathbf{M}^-\mathbf{C}^{k-1} + \mathbf{M}^0\mathbf{C}^k + \mathbf{M}^+\mathbf{C}^{k+1}] \tag{35}$$

for $k = -N_e + 2, -N_e + 3, \ldots, N_e - 1$, where $\mathbf{C}^k$ is a column vector that contains all expansion coefficients of solution in the element with index k, and $\Delta x_k = \Delta x_c$ and Δx_f for the elements in coarse and fine meshes respectively. $\mathbf{M}^0$, $\mathbf{M}^-$ and $\mathbf{M}^+$ are the coefficient matrices for the dominant element and its left and right adjacent elements respectively. For the first and the last element, due to periodic boundary condition, we have

$$\frac{d\mathbf{C}^{-N_e+1}}{dt} = \frac{1}{\Delta x_c}[\mathbf{M}^-\mathbf{C}^{N_e} + \mathbf{M}^0\mathbf{C}^{-N_e+1} + \mathbf{M}^+\mathbf{C}^{-N_e+2}] \tag{36}$$

and

$$\frac{d\mathbf{C}^{N_e}}{dt} = \frac{1}{\Delta x_f}[\mathbf{M}^-\mathbf{C}^{N_e-1} + \mathbf{M}^0\mathbf{C}^{N_e} + \mathbf{M}^+\mathbf{C}^{-N_e+1}]. \tag{37}$$

The above can be easily written in a block-matrix form as

$$\frac{d\overline{\mathbf{C}}}{dt} = \mathrm{diag}(\Delta x_k^{-1}\mathbf{I}_N)\cdot \begin{bmatrix} \mathbf{M}^0 & \mathbf{M}^+ & \mathbf{0} & \mathbf{0} & \cdot & \cdot & \mathbf{M}^- \\ \mathbf{M}^- & \mathbf{M}^0 & \mathbf{M}^+ & \mathbf{0} & \cdot & \cdot & \mathbf{0} \\ \mathbf{0} & \mathbf{M}^- & \mathbf{M}^0 & \mathbf{M}^+ & \cdot & \cdot & \mathbf{0} \\ \cdot & \cdot & \cdot & \cdot & \cdot & \cdot & \cdot \\ \cdot & \cdot & \cdot & \cdot & \cdot & \cdot & \cdot \\ \mathbf{0} & \cdot & \cdot & \mathbf{0} & \mathbf{M}^- & \mathbf{M}^0 & \mathbf{M}^+ \\ \mathbf{M}^+ & \cdot & \cdot & \mathbf{0} & \mathbf{0} & \mathbf{M}^- & \mathbf{M}^0 \end{bmatrix} \overline{\mathbf{C}} \equiv \overline{\mathbf{H}\mathbf{C}} \tag{38}$$

where $\overline{\mathbf{C}}$ is a column vector of length $N_g = N \cdot 2N_e$ containing all expansion coefficients on the whole grid, and N is the degree of freedom in one element. Thus $\overline{\mathbf{C}}$ is of the form

$$\overline{\mathbf{C}} = \begin{bmatrix} \mathbf{C}^{-N_e+1} \\ \mathbf{C}^{-N_e+2} \\ \cdot \\ \cdot \\ \cdot \\ \mathbf{C}^{N_e} \end{bmatrix}, \quad \text{with } \mathbf{C}^k = \begin{bmatrix} c_1^k \\ c_2^k \\ \cdot \\ \cdot \\ \cdot \\ c_N^k \end{bmatrix}, \quad k = -N_e + 1, \ldots, N_e.$$

4.1. Analysis of RKDG with uniform time step

We first present a study of stability analysis with a uniform time step. For the semi-discrete equation (38), the Runge–Kutta scheme can be expressed as

$$\mathbf{K}_1 = \overline{\mathbf{H}}\overline{\mathbf{C}}^n, \tag{39}$$

$$\mathbf{K}_2 = \overline{\mathbf{H}}(\overline{\mathbf{C}}^n + \Delta t a_{21}\mathbf{K}_1), \tag{40}$$

$$\cdots\cdots \tag{41}$$

$$\mathbf{K}_p = \overline{\mathbf{H}}(\overline{\mathbf{C}}^n + \Delta t[a_{p1}\mathbf{K}_1 + \cdots + a_{pp-1}\mathbf{K}_{p-1}]), \tag{42}$$

$$\overline{\mathbf{C}}^{n+1} = \overline{\mathbf{C}}^n + \Delta t[b_1\mathbf{K}_1 + b_2\mathbf{K}_2 + \cdots + b_p\mathbf{K}_p]. \tag{43}$$

From the above, it is straightforward to get a matrix relation

$$\overline{\mathbf{C}}^{n+1} = \mathbf{R}\overline{\mathbf{C}}^{n}. \tag{44}$$

Matrix **R** will be referred to as the amplification matrix. The scheme would be stable if all eigenvalues of **R** have a modulus less or equal to unity, i.e.

$$\max(|\lambda_i|) \leqslant 1, \tag{45}$$

where $|\lambda_i|$ is the modulus of the eigenvalue of **R**.

Obviously, the amplification matrix **R** is dependent on the specific RK scheme, Courant–Friedrichs–Lewy condition (CFL) and the spacings of the coarse and fine element. Here we first present results for a uniform grid with $\Delta x_c = \Delta x_f = 1$ (Case 1) as well as a nonuniform grid with $\Delta x_c = 1$, $\Delta x_f = 1/2$ (Case 2) but with a single uniform time step. Fig. 5 show eigenvalue distribution of the fourth-order DG scheme coupled with LDDRK5, where the CFL number is at the stability limit. The eigenvalue distributions of LDDRK4-DG and LDDRK6-DG are found in the similar form. The CFL number is defined by the coarse mesh as

$$\mathrm{CFL} = q\frac{\Delta t_c}{\Delta x_c}. \tag{46}$$

For LDDRK schemes and DG schemes up to $P = 6$, the stability limits on the CFL number determined by condition (45) have been found computationally and given in Table 2 for case 1, for several LDDRK schemes and DG schemes. The stability limits obtained by direct numerical simulation are also listed. Very good agreement is observed.

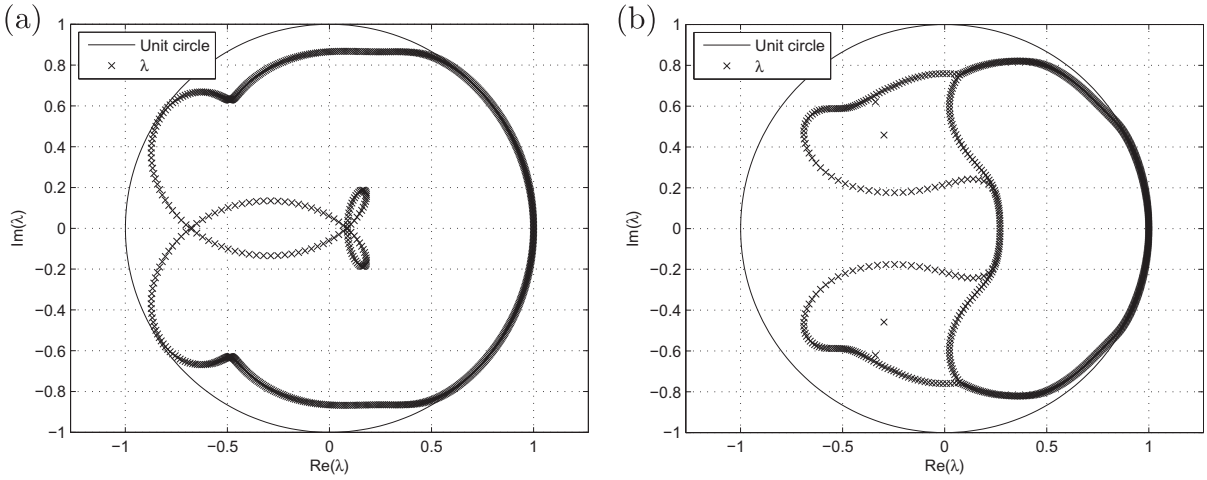

Fig. 5. Distribution of eigenvalues of the amplification matrix **R** for uniform time-step LDDRK5-DG($\mathcal{O}(4)$): (a) Case 1 when CFL = 0.218 and (b) Case 2 when CFL = 0.109.

Table 2
Stability limits for uniform LDDRK-DG with $\theta = 0.5$.

Stage of LDDRK	Order of DG	CFL_{max}	
		Analysis	Numerical
4	1	2.29	2.29
	2	0.646	0.646
	3	0.329	0.329
	4	0.202	0.202
	5	0.138	0.137
	6	0.100	0.100
5	1	2.73	2.72
	2	0.708	0.709
	3	0.356	0.358
	4	0.218	0.219
	5	0.148	0.149
	6	0.107	0.107
6	1	3.10	3.11
	2	0.825	0.825
	3	0.410	0.411
	4	0.252	0.253
	5	0.172	0.172
	6	0.124	0.125

4.2. Analysis of RKDG with nonuniform time step

We now consider the stability for the proposed nonuniform time-step RK schemes. By applying the coupled Runge–Kutta scheme (11)–(13) to the semi-discrete equation (38), together with coupling matrices developed in (16), (17) and (20), a matrix relation of the form (44) can again be obtained,

$$\overline{\mathbf{C}}^{n+1} = \mathbf{R}(\Delta t_c, \Delta t_f)\overline{\mathbf{C}}^{n}, \tag{47}$$

where the amplification matrix $\mathbf{R}$ now depends on the time steps Δt_c and Δt_f of the coarse and fine meshes.

We consider the ratio $\Delta t_c{:}\Delta t_f = \Delta x_c{:}\Delta x_f = 2{:}1$ (Case 3), so that CFL number is uniform on the entire domain. Obviously, the eigenvalues of $\mathbf{R}(\Delta t_c, \Delta t_f)$ for a nonuniform time step will differ from those for a uniform time step considered in 4.1. We have tried to plot the eigenvalues of $\mathbf{R}$ for LDDRK-DG($\mathcal{O}(1-6)$) at the corresponding maximal CFL number obtained in the same way as in the previous section. For comparing with the results of Case 1 and Case 2, distributions of the eigenvalues of Case 3 that take non-uniformity of time-step size and element-spacing size into account. Fig. 6 shows the distributions of the eigenvalues for LDDRK5-DG as an example. Those maximal CFL numbers for nonuniform LDDRK-DG schemes are in a good agreement with the stability limits obtained in direct numerical simulation, given as in Table 3. It is observed that the stability limits in nonuniform time-step cases remain the same or are slightly larger than those of uniform LDDRK-DG schemes in

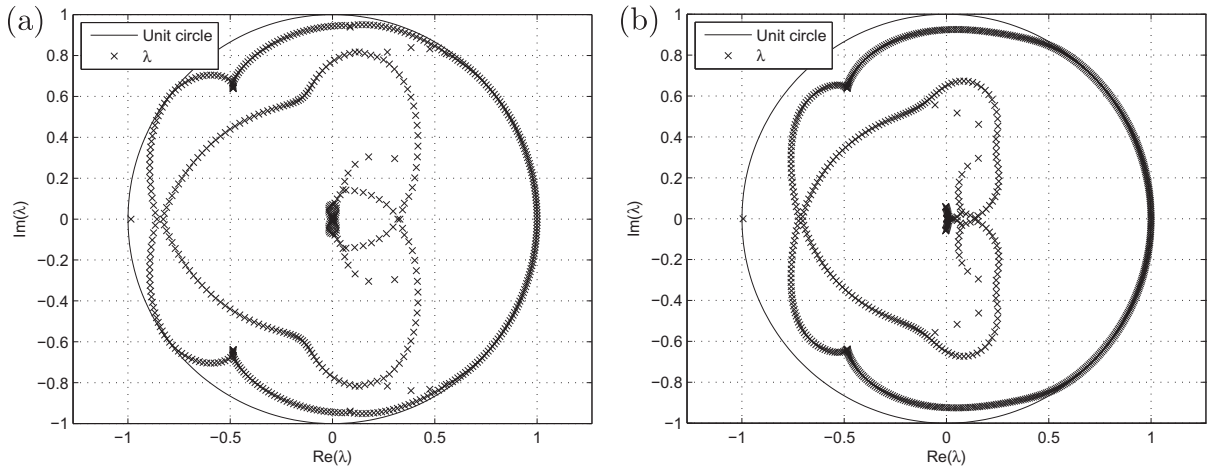

Fig. 6. Distribution of eigenvalues of the amplification matrix $\overline{\mathbf{R}}$ for nonuniform time-step LDDRK5-DG: (a) LDDRK5-DG($\mathcal{O}(3)$) when CFL = 0.365 and (b) LDDRK5-DG($\mathcal{O}(4)$) when CFL = 0.214.

Table 3
Stability limits for nonuniform LDDRK-DG with $\Delta t_c{:}\Delta t_f = 2{:}1$.

Stage of LDDRK	Order of DG	CFL_{max}	
		Analysis	Numerical
4	1	2.31	2.31
	2	0.659	0.659
	3	0.334	0.334
	4	0.204	0.204
	5	0.138	0.135
	6	0.100	0.100
5	1	2.76	2.76
	2	0.719	0.719
	3	0.365	0.364
	4	0.214	0.214
	5	0.139	0.139
	6	0.0982	0.0982
6	1	3.08	3.08
	2	0.832	0.832
	3	0.417	0.417
	4	0.255	0.254
	5	0.173	0.173
	6	0.125	0.125

Note. Upwind-parameter $\theta = 0.5$.

Table 2, except when the order of DG scheme is higher than 3 and in combination with LDDRK5, where the stability limits of nonuniform time-step for LDDRK5-DG schemes drop down slightly. As such, use of coupling procedures is not expected to have a negative impact on the stability limit of RKDG schemes in general.

5. Numerical examples

In this section, we present numerical examples of applying the nonuniform time step Runge–Kutta scheme developed in the previous sections. One-dimensional test examples are shown in Section 5.1 and two-dimensional examples are shown in Section 5.2.

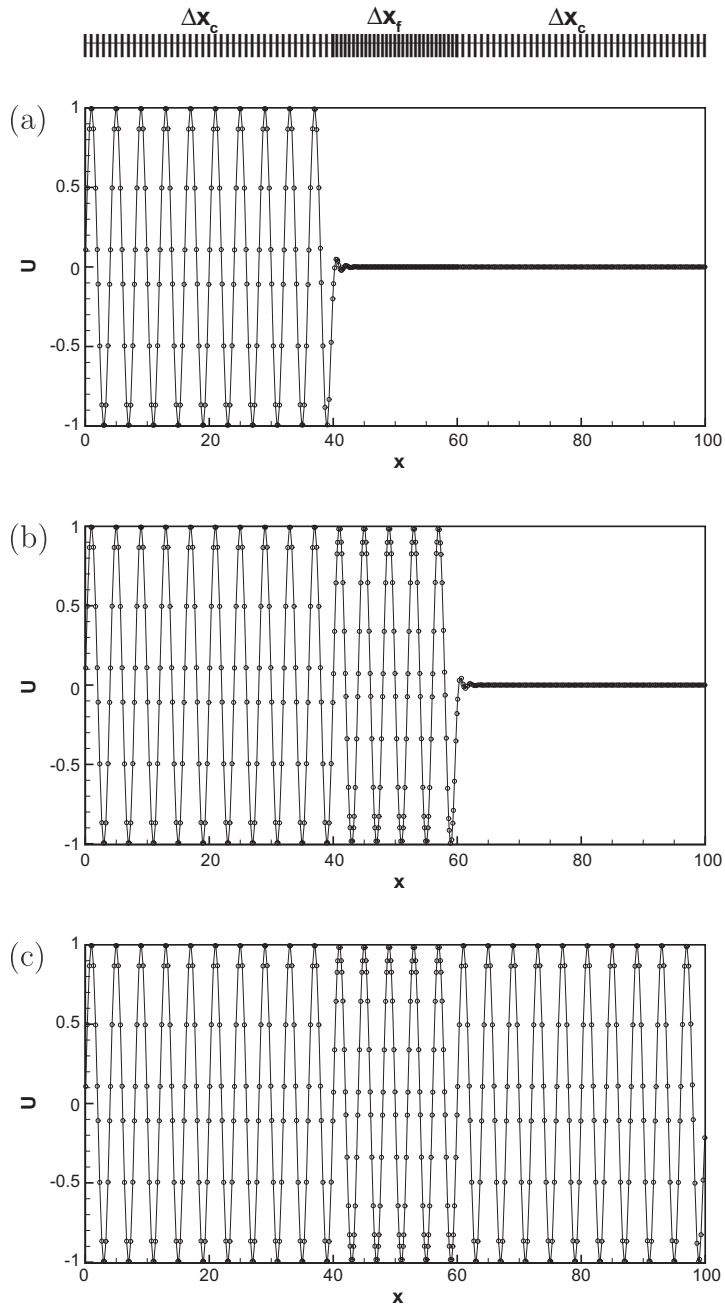

Fig. 7. Solution at (a) $t = 40$, (b) $t = 60$ and (c) $t = 100$ when $\Delta t_1 : \Delta t_2 : \Delta t_3 = 3:2:3$.

5.1. One-dimensional tests

5.1.1. Linear case

The first case is the one-dimensional scalar transport equation

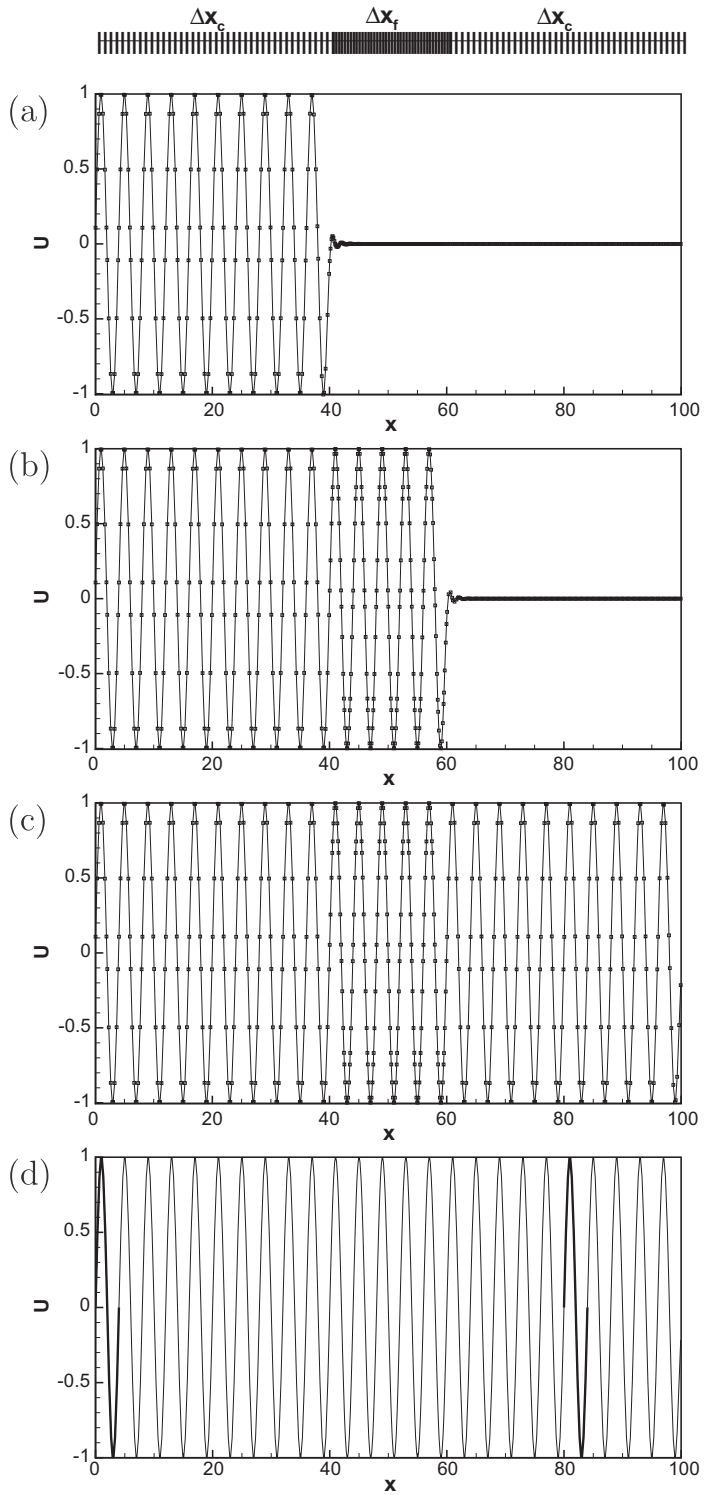

Fig. 8. Solution at (a) $t = 40$, (b) $t = 60$ and (c) $t = 100$, when $\Delta t_1{:}\Delta t_2{:}\Delta t_3 = 2{:}1{:}2$; and (d) the 1st and 20th periods at $t = 100$.

$$\frac{\partial u}{\partial t}+\frac{\partial u}{\partial x}=0 \tag{48}$$

with the initial condition $u(x,0)=0$, on the interval $x\in[0,100]$. At the boundary $x=0$, a sine wave $u(0,t)=\sin\left(\frac{\pi}{2}t\right)$ is excited which propagates into the domain. We consider a nonuniform grid consisting of three blocks, with intervals [0,40], [40,60], and [60,100], of which the second one is fine mesh and the other two are coarse meshes. The one-dimensional version of nonuniform time-step RKDG method is used to solve this problem. With a uniform CFL number, the time-step sizes of the neighboring blocks are different. Thus the coupling procedure should be adopted in the elements adjacent to the interfaces of fine and coarse meshes.

Fourth-order low-storage LDDRK scheme and corresponding coupling procedures are applied here combined with the same order DG method. The numerical solutions u_h are given when $\Delta x_c:\Delta x_f=3:2$ (Case 1A) in Fig. 7, and $\Delta x_c:\Delta x_f=2:1$ (Case 1B) in Fig. 8 respectively where $\Delta x_c=1$ for both cases, and the grids are illustrated on the top of the graphs. In both examples, the sine wave propagates through the interfaces without any noticeable error.

The accuracy of the solution is further analyzed in a grid refinement study. We compare the numerical solution of the 20th period with the 1st period at $t=100$ in the L_2-norm of the error which is defined as

$$E=\sqrt{\int_0^{\lambda}|u_h(x,t)-u_h(x+20\lambda,t)|^2\,\mathrm{d}x}\quad=\sqrt{\frac{h}{2}\sum_{n=0}^{n_0-1}\int_{-1}^{1}|u_h^n(\xi,t)-u_h^{n+20n_0}(\xi,t)|^2\,\mathrm{d}\xi}. \tag{49}$$

The grid refinement results are shown in Table 4 for case 1B. The super-convergence rates are observed when the accuracy order of DG ranges from 2 to 6. Also shown are the results by a single uniform time step. The comparison between the results by using nonuniform time step with those by using single time step implies that the accuracy of the solution is not reduced by the present coupling procedures, and the nonuniform time-step Runge–Kutta integration preserves the super-convergence property of DG method [20,1].

5.1.2. Burger's equation

In this example, the coupling procedure is applied to a nonlinear test problem. Consider one-dimensional Burger's equation written in the first-order system

$$\begin{aligned}&\frac{\partial u}{\partial t}+\frac{\partial(u^2/2)}{\partial x}+\epsilon\frac{\partial v}{\partial x}=0,\\&v+\frac{\partial u}{\partial x}=0\end{aligned} \tag{50}$$

with a smooth initial condition

Table 4
Error E on nonuniform grids with $\Delta x_c:\Delta x_f=2:1$ at $t=100$.

P	Δx_c	$\Delta t_c:\Delta t_f=2:1$		$\Delta t_c:\Delta t_f=1:1$	
		Error E	Order	Error E	Order
1	1.0	0.1337986E+01		0.1337986E+01	
	0.5	0.8928877E+00	0.5835	0.8928877E+00	0.5835
	0.25	0.1943643E+00	2.1997	0.1943643E+00	2.1997
	0.125	0.2802999E−01	2.7937	0.2802999E−01	2.7937
	0.0625	0.3615612E−02	2.9547	0.3615612E−02	2.9547
2	1.0	0.1555250E+00		0.1555260E+00	
	0.5	0.3406188E−02	5.5128	0.3406192E−02	5.5129
	0.25	0.9236151E−04	5.2047	0.9236102E−04	5.2047
	0.125	0.2770594E−05	5.0590	0.2770156E−05	5.0592
	0.0625	0.8563485E−07	5.0159	0.8714656E−07	4.9904
3	1.0	0.2034853E−02		0.2034971E−02	
	0.5	0.2606452E−04	6.2867	0.2606921E−04	6.2865
	0.25	0.2496610E−06	6.7060	0.2498732E−06	6.7050
	0.125	0.2092026E−08	6.8989	0.2126499E−08	6.8766
4	2.0	0.1237796E−01		0.1238349E−01	
	1.0	0.1594024E−04	9.6009	0.1609385E−04	9.5877
	0.5	0.1554066E−07	10.0024	0.1928697E−07	9.7047
5	4.0	0.2294258E+00		0.2290161E+00	
	2.0	0.6976945E−04	11.6831	0.7423456E−04	11.5911

Note. Δt_f are of the same value in two cases above.

$$u(x,0) = 1 - \tanh\left(\frac{x - x_0}{2\epsilon}\right),$$
$$v(x,0) = \left(-1 + \tanh^2\left(\frac{x - x_0}{2\epsilon}\right)\right)\Big/2\epsilon,$$

where $x \in [0,50]$, and $x_0 = 4$. $\epsilon = 0.2$ is the viscous coefficient.

A general two-block grid is also applied here, with intervals [0,25] and [25,50], of which the first block has a coarse spacing $\Delta x_c = 1$ and $\Delta x_c{:}\Delta x_f = 2{:}1$. The interface of two blocks locates at $x = 25$ that is denoted in Fig. 9. With the uniform CFL number the time-step ratio is $\Delta t_c{:}\Delta t_f = 2{:}1$. Fourth-order low-storage LDDRK scheme combined with fourth-order DG discretization is used. The values of u and v are both required to be coupled properly at the interface of two meshes.

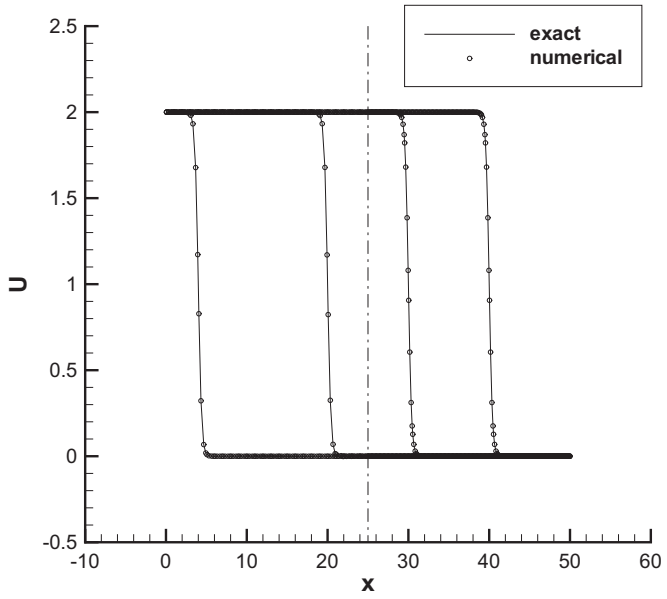

(a)

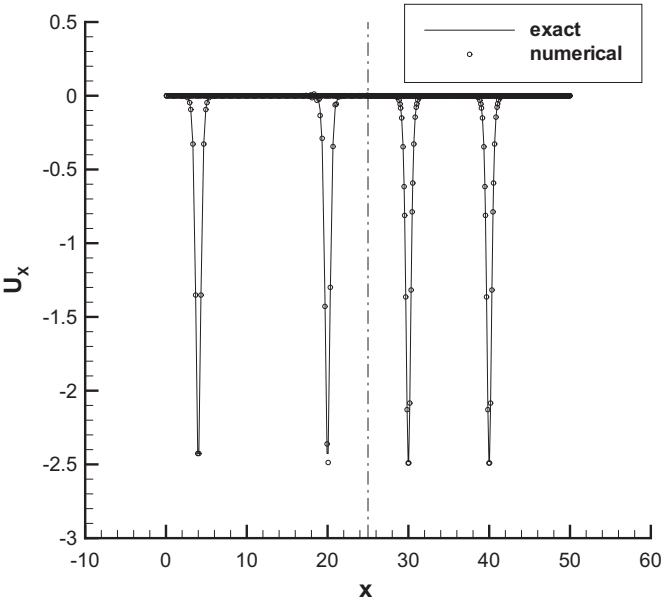

(b)

Fig. 9. Solutions U and $\frac{\partial U}{\partial x}$ of Burger's equation at $t = 0$, 16, 26, and 36; the dashdotted line locates the interface of meshes.

The numerical solutions and its first spatial derivative on nonuniform grid are compared with the exact solutions in Fig. 9, which keeps the same shape as the initial condition as it propagates downstream. No oscillation is observed in the neighborhood of the interface at $x = 25$. By comparing with solutions obtained by a single time step, the accuracy of the solution is also found to be unaffected by the coupling procedures in the current case.

5.2. Two-dimensional test

5.2.1. Acoustic wave in free field

For two-dimensional verification, the coupling procedure is applied to simulate the propagation of a Gaussian pulse in a free field at first, using the linearized Euler equations in the domain $x \in [-100, 100]$, $y \in [0, 200]$

$$\frac{\partial \mathbf{U}}{\partial t} + \mathbf{A}\frac{\partial \mathbf{U}}{\partial x} + \mathbf{B}\frac{\partial \mathbf{U}}{\partial y} = 0, \tag{51}$$

where

$$\mathbf{U} = \begin{bmatrix} \rho' \\ u' \\ v' \\ p' \end{bmatrix}, \quad \mathbf{A} = \begin{bmatrix} u_o & \rho_o & 0 & 0 \\ 0 & u_o & 0 & 1/\rho_o \\ 0 & 0 & u_o & 0 \\ 0 & \gamma p_o & 0 & u_o \end{bmatrix}, \quad \mathbf{B} = \begin{bmatrix} v_o & 0 & \rho_o & 0 \\ 0 & v_o & 0 & 0 \\ 0 & 0 & v_o & 1/\rho_o \\ 0 & 0 & \gamma p_o & v_o \end{bmatrix}.$$

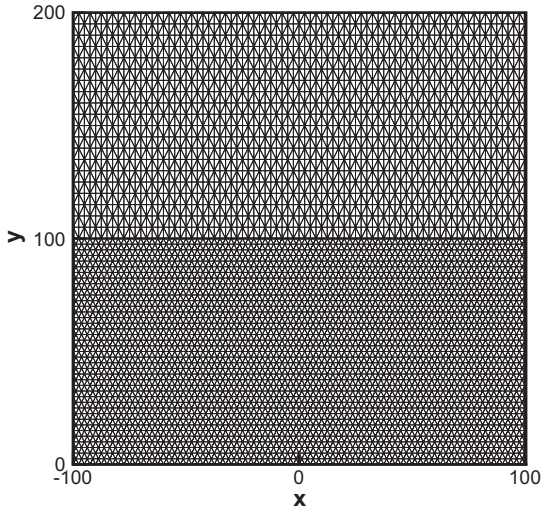

(a)

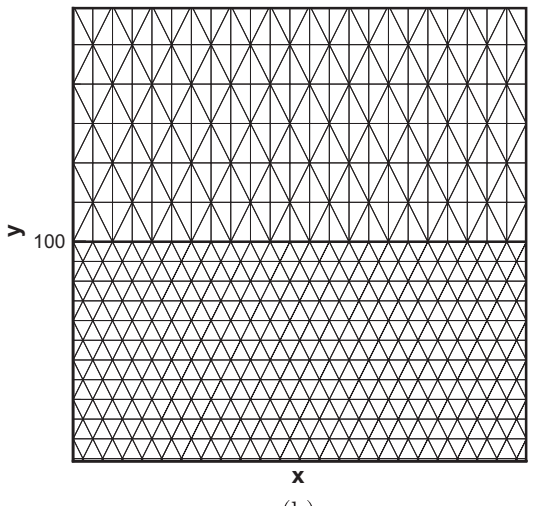

(b)

Fig. 10. 2D nonuniform grid: (a) whole and (b) local.

The background flow parameters $(\rho_o, u_o, v_o, p_o)^T$ are constant

$$\begin{aligned} p_o &= 1/\gamma, \\ \rho_o &= 1, \\ u_o &= v_o = 0. \end{aligned} \tag{52}$$

Here, $\gamma = 1.4$. And the perturbing quantities $(\rho',\ u', v', p')^T$ have the initial profile

$$\rho' = p' = \exp\left\{-(\ln 2)\left[\frac{x^2 + (y-125)^2}{r_o^2}\right]\right\},$$
$$u' = v' = 0, \quad r_o = 10.$$

The linear coupling procedure is tested on the nonuniform triangular grid as shown in Fig. 10, which consists of two blocks with different characteristic lengths of the elements that satisfy h_c:h_f = 2:1.

Contours of pressure at time t = 30, 45, 60, and 75 are given in Fig. 11. The pulse propagates smoothly from the coarse mesh to the fine mesh. The comparisons of the numerical solutions with the exact one along the line x = 0 perpendicular to the interface of two blocks are shown in Fig. 12 with excellent agreements. In consideration of more elements neighboring the interface of the blocks in 2D problems, it is reasonable that the overhead due to the coupling procedures are slightly more in 2D problems than that in 1D problems.

5.2.2. Acoustic wave scattering off single circular cylinder

After the validation of the developed coupling procedures on 2D nonuniform triangular grid for a Gaussian pulse in the free field, we further consider the acoustic wave scattered by a circular cylinder of the radius r = 0.5, which was a benchmark problem of the second CAA workshop [37]. The acoustic wave is initialized by the pressure pulse

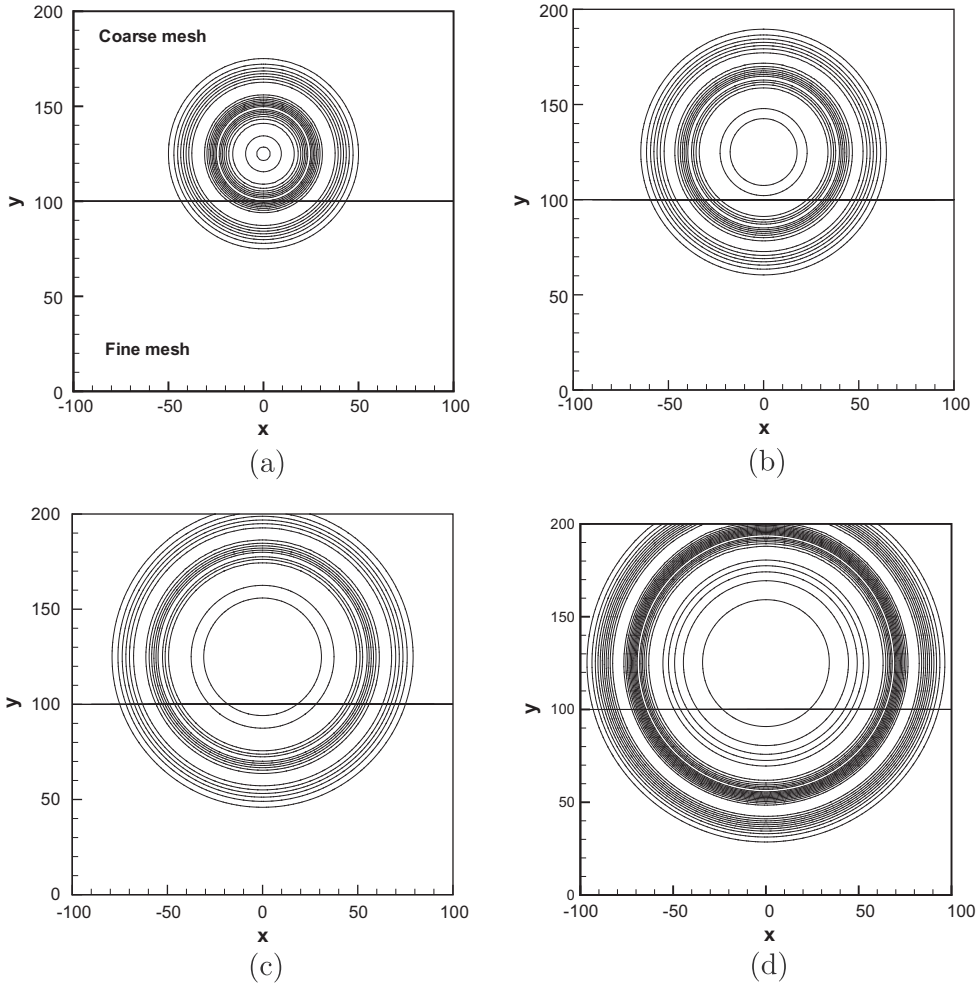

Fig. 11. Contours of pressure at t = 30, 45, 60 and 75 with M_x = 0, and M_y = 0.

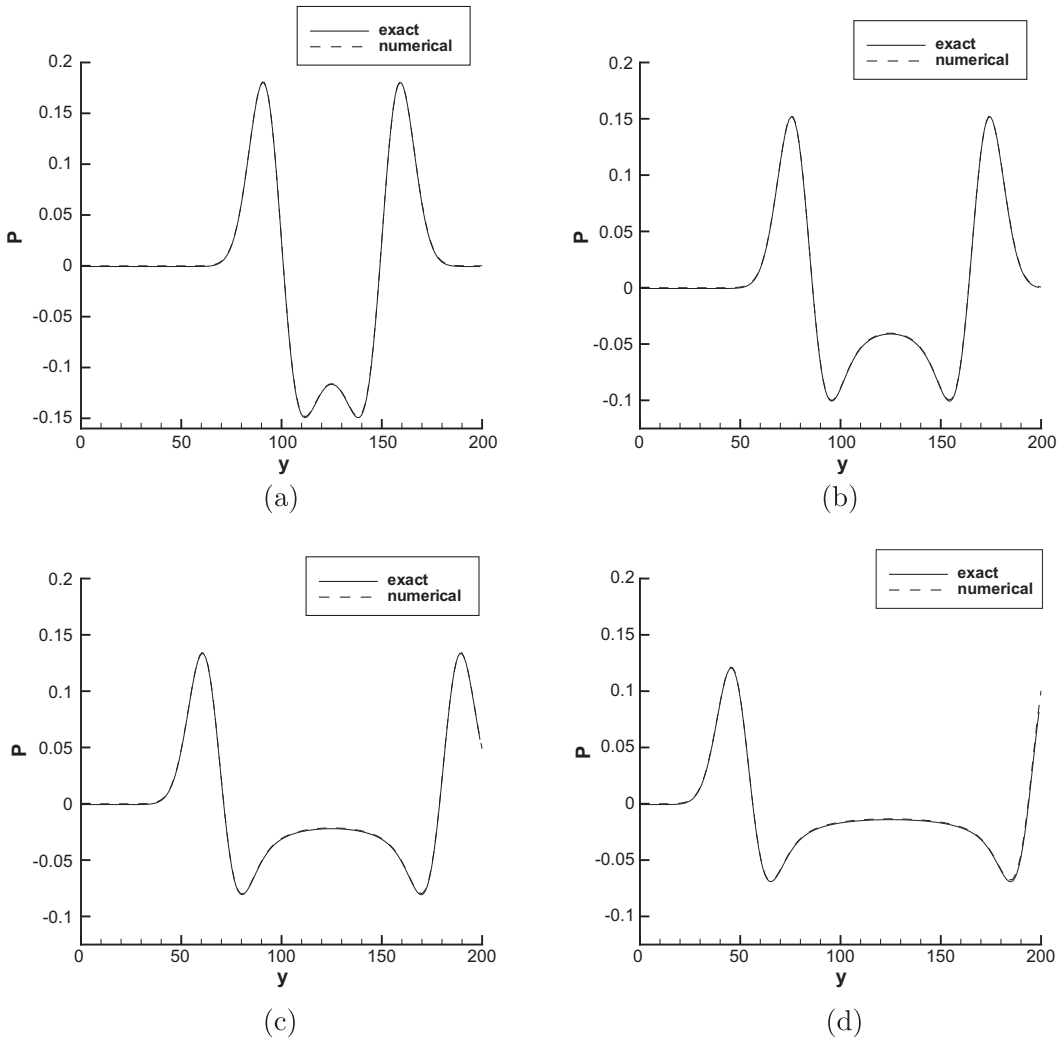

Fig. 12. Pressure on the line $x = 0$ at $t = 30$, 45, 60 and 75.

$$p = \exp\left[-\ln(2)\frac{(x-4)^2+y^2}{0.2^2}\right] \tag{53}$$

and the linearized Euler equation (51) is solved. Fifth-order DG spatial discretization and fourth-order LDDRK6 are applied here. The computational domain is $x \in [-10,10]$,$y \in [-10,10]$. The whole domain is discretized by unstructured triangular grid. In order to resolve the curved wall boundary of the cylinder, the finest grid is used in a small annular area ($0.5 \leqslant r \leqslant 1.0$) around the cylinder, which is denoted as Block 1 in Fig. 13. The wall boundary is approximated by 40 straight-edged elements. A relatively larger area away from the cylinder ($1.0 \leqslant r \leqslant 5.5$) is Block 2. The grid in this block is generated to ensure that the characteristic length of the elements is less than 0.167, so the equivalent points-per-wave (PPW) with respect to fifth-order DG is great than 6. The rest of the domain is denoted as Block 3, in which the grid is coarsened as it is far away from the cylinder. For non-reflecting boundary of the computational domain, the Perfectly Matched Layer boundary condition (PML) [24] is applied. The width of PML area indicated as Block 4 is $D = 2$, and quadrilateral elements are used in this area. The blocks 1–4 contain 452, 7206, 8208, and 704 elements, respectively. The local time steps used in every block satisfy $\Delta t_1 : \Delta t_2 : \Delta t_3 : \Delta t_4 = 1:2:4:4$, and $\Delta t_1 = 0.025$. Fig. 14 shows the pressure contours at $t = 8$, and the comparisons of the pressure at three points of which the polar coordinates are A ($r = 5$, $\theta = \pi/2$), B ($r = 5$, $\theta = 3\pi/4$) and C ($r = 5$, $\theta = \pi$) as a function of time show a good agreement with the exact solution in Fig. 15.

5.3. Reduction in computational cost

In this section, we examine the reduction in computational cost due to the use of nonuniform time steps. We first give an estimate on the time reduction factor without including the cost of the coupling procedures. Let $N_{e,i}$ denote the number of

elements advanced with time step Δt_i. Then the computational cost, excluding that of interface coupling for the moment, will be proportional to

$$T_m = \sum_{i=1}^{M} N_{e,i} \frac{t'}{\Delta t_i}, \tag{54}$$

where t' is the final time of computation and M is the number of blocks with different time steps used in the computation. On the other hand, if the smallest time step is used for all the elements, the computational cost will be proportional to

$$T_s = \sum_{i=1}^{M} N_{e,i} \frac{t'}{\min\limits_{1 \leqslant i \leqslant M} (\Delta t_i)}, \tag{55}$$

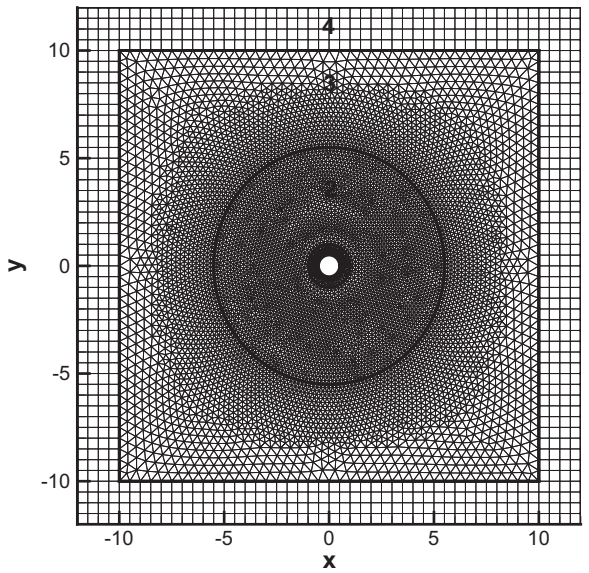

(a)

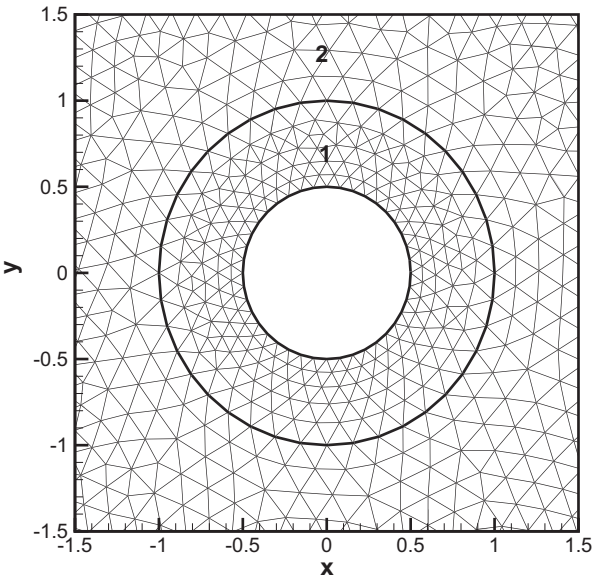

(b)

Fig. 13. 2D multi-block grid around a cylinder: (a) whole domain and (b) local grid around cylinder.

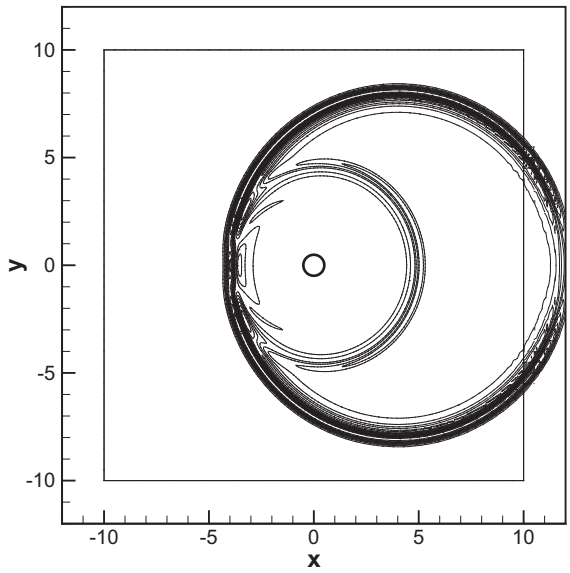

Fig. 14. Pressure contours at $t = 8$.

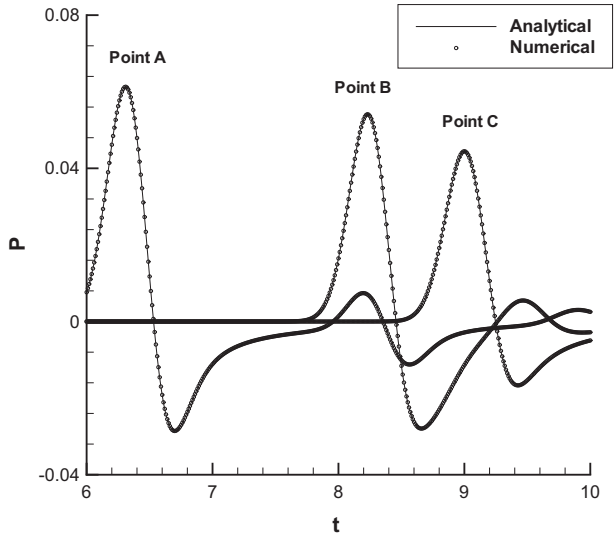

Fig. 15. Time history of the pressure at point A ($r = 5$, $\theta = \pi/2$), B ($r = 5$, $\theta = 3\pi/4$) and C ($r = 5$,$\theta = \pi$) as indicated.

where $\min_{1 \leqslant i \leqslant M}(\Delta t_i)$ is the smallest time step allowed for the entire computational domain. Then a computational time reduction factor can be defined as

$$S = 1 - \frac{T_m}{T_s}. \tag{56}$$

Clearly, the degree of time reduction that can be achieved by using multirate time integration depends on the relative distribution of the number of elements among the various time steps. The smaller a percentage of the finest elements, the greater a reduction factor in the computational time.

This computational cost reduction factor S for all the numerical examples considered in this section are shown in Table 5. To account for the additional costs incurred by the coupling procedures at the interfaces of different time steps, all the examples have been re-run with a single (smallest) time step and an actual computational cost reduction factor is calculated for each test case,

Table 5
Computational cost saving by variable time step algorithm.

Examples	5.1.1(1A)	5.1.1(1B)	5.1.2	5.2.2	5.2.2
S (%)	24.2	33.3	33.3	33.3	62.1
S^* (%)	13.3	32.1	15.7	20.9	54.5

Note. S is the estimated value, and S^* is the numerical value.

$$S^* = 1 - \frac{T_m^*}{T_s^*}, \tag{57}$$

where T_m^* and T_s^* are the actual computational times using multirate and single time step integrations respectively. It is encouraging to see that for the practical problem of sound scattering by a cylinder, a time reduction over 50% is achieved with a relatively small cost for the coupling procedures.

6. Conclusions

For complex physical problems, the application of Runge–Kutta discontinuous Galerkin method with a uniform time step is often constrained by the limitation on the time step afforded by the CFL condition based on the smallest elements. In this paper, high-order Runge–Kutta scheme with nonuniform time-step sizes is developed which makes the time integration of semi-discrete systems on nonuniform grid more efficient. The formulation of linear coupling procedure is derived based on the general explicit p-stage Runge–Kutta formulas, and it can be easily extended to Runge–Kutta schemes used frequently in CAA. The coupling procedure is only necessary for the elements neighboring the interface of two meshes advancing with different time-step sizes. An approach of optimization for the coupling coefficients is also carried out for low dissipation and low dispersion errors. Moreover, stability of the coupling procedure has also been examined for LDDRK schemes in combination with DG method up to sixth order. It was found that the coupling procedures for nonuniform time-step LDDRK-DG schemes generally preserve the stability property of uniform time step integration. For validation, numerical experiments have been performed on one- and two-dimensional problems. The numerical results illustrate the stability and accuracy properties of proposed coupling procedures. Furthermore, applicability of the linear procedure to nonlinear problem is also demonstrated by solving the Burger's equation. In addition, the benefits in computational cost saving by the presented algorithm are discussed. Comparing with the computational cost by single time step integration, the developed algorithm results in obvious benefits in computational efficiency for linear problems, and it also works for the nonlinear one. The overhead due to the coupling procedures is limited, though that is a slightly higher in solving nonlinear Burger's equation than in linear cases. More applications of the algorithm to complex acoustic problems will be investigated in the future work.

Acknowledgments

This work is supported by grants from the National Natural Science Foundation of China 50890181 and 50676003, the 973 Program-2007CB714604 (Li Liu and Xiaodong Li) and the National Science Foundation DMS-0810946 (Fang Q. Hu). Li Liu would like to acknowledge the support from China Scholarship Council which renders her stay at the Old Dominion University through 2007–2008. The authors also would like to acknowledge the 111 Projects B07009 and B08009 of China. Many thanks to the reviewers for their helpful comments.

Appendix A. Extension to Runge–Kutta schemes frequently used in CAA

In this Appendix, we will show more details about the extension of the coupling procedures presented in Section 3 to TVD, 2N-storage and minimum storage Runge–Kutta schemes.

A.1. TVD Runge–Kutta schemes

Third-order TVD Runge–Kutta time integration is used frequently for hyperbolic cases for the property of total variation diminishing and strong stability [18], especially the ones involving shocks. The general form of the scheme is as followed,

$$\begin{aligned} &\mathbf{U}^{(0)} = \mathbf{U}^n, \\ &\mathbf{U}^{(i)} = (1-\beta_i)\mathbf{U}^{(0)} + \beta_i(\mathbf{U}^{(i-1)} + \Delta t F(\mathbf{U}^{(i-1)})), \\ &\quad i = 1,\ldots,m, \\ &\mathbf{U}^{(n+1)} = \mathbf{U}^m. \end{aligned} \tag{58}$$

For third-order TVD Runge–Kutta scheme ($m = 3$),

$$\beta_1 = 1, \quad \beta_2 = 1/4, \quad \beta_3 = 2/3.$$

To derive the coupling coefficient matrices, we rewrite it into the general m-stage Runge–Kutta form (9), and the corresponding coefficients are,

$$\begin{aligned} &a_{21} = 1, \\ &a_{31} = 1/4, \quad a_{32} = 1/4, \\ &b_1 = 1/6, \quad b_2 = 1/6, \quad b_3 = 2/3. \end{aligned} \tag{59}$$

The coefficient matrices for coupling procedures can be obtained by formulae (14)–(20) in Section 3.

A.2. 2N-Storage LDDRK Schemes

For efficient implementation of linear problems, LDDRK schemes are usually rewritten into special forms that require low-storage, such as 2N-storage schemes, where N is the number of degrees of freedom of the system.

2N-storage implementation is usually executed in the following way

$$\begin{aligned} &\mathbf{W}_i = \alpha_i \mathbf{W}_{i-1} + hF(\mathbf{U}_{i-1}), \\ &\mathbf{U}_i = \mathbf{U}_{i-1} + \beta_i \mathbf{W}_i, \\ &\quad i = 1, \ldots, p, \end{aligned} \tag{60}$$

where $\mathbf{U}_0 = \mathbf{U}^{n-1}$ and $\mathbf{U}^n = \mathbf{U}_p$; α_i and β_i are the coefficients given in [36].

Then matrix $\mathbf{C}$ in coupling procedures is of the form

$$\begin{bmatrix} c_{11} & 0 & 0 & \cdot & \cdot & 0 \\ c_{21} & c_{22} & 0 & \cdot & \cdot & 0 \\ c_{31} & c_{32} & c_{33} & \cdot & \cdot & 0 \\ \cdot & \cdot & \cdot & \cdot & \cdot & \cdot \\ \cdot & \cdot & \cdot & \cdot & \cdot & \cdot \\ c_{p1} & c_{p2} & c_{p3} & \cdot & \cdot & c_{pp} \end{bmatrix}, \tag{61}$$

where

$$\begin{aligned} &c_{11} = 1, \\ &c_{21} = 1 + \alpha_2 c_{11}, && c_{22} = \beta_1 c_{11}, \\ &c_{31} = 1 + \alpha_3 c_{21}, && c_{32} = \beta_1 c_{11} + \beta_2 c_{21} + \alpha_3 c_{22}, \\ &c_{33} = \beta_2 c_{22}, \\ &c_{41} = 1 + \alpha_4 c_{31}, && c_{42} = \beta_1 c_{11} + \beta_2 c_{21} + \beta_3 c_{31} + \alpha_4 c_{32}, \\ &c_{43} = \beta_2 c_{22} + \beta_3 c_{32} + \alpha_4 c_{33}, && c_{44} = \beta_3 c_{33}, \\ &\cdots\cdots \\ &c_{p1} = 1 + \alpha_p c_{p-11}, && c_{p2} = \beta_1 c_{11} + \beta_2 c_{21} + \cdots + \beta_{p-1} c_{p-11} + \alpha_p c_{p-12}, \\ &\cdots \\ &c_{pp} = \beta_{p-1} c_{p-1p-1}, \end{aligned} \tag{62}$$

A.3. Minimum storage Runge–Kutta schemes

Most recently, a new minimum storage Runge–Kutta scheme of fourth-order accuracy with six stages is proposed by M. Calvo and his co-workers in [4], which only requires 2N-storage with low dissipation and low dispersion errors. This algorithm can be written equivalently as the p-stage Runge–Kutta schemes

$$\begin{aligned} &F_1 = F(\mathbf{U}^n), \\ &F_i = F(\mathbf{U}^n + \Delta t \sum_{j=1}^{i-1} b_j F_j + \Delta t \gamma_{i-1} F_{i-1}), \quad (i = 2, \ldots, p), \\ &\mathbf{U}^{n+1} = \mathbf{U}^n + \Delta t \sum_{i=1}^{p} b_i F_i. \end{aligned} \tag{63}$$

Thus, the coupling matrix $\mathbf{C}$ has the same form as in formula (14), but the entries become

$$
\begin{aligned}
&c_{22} = b_1 + \gamma_1,\\
&c_{32} = b_1 + b_2 + \gamma_2, \quad c_{33} = (b_2 + \gamma_2)(b_1 + \gamma_1),\\
&\cdots\cdots\\
&c_{p2} = \sum_{i=1}^{p} b_i + \gamma_{p-1}, \quad c_{p3} = \sum_{i=2}^{p-1} b_i c_{i2} + \gamma_{p-1} c_{p-12},\\
&\cdots\\
&c_{pp} = \prod_{i-1}^{p-1} (b_i + \gamma_i),
\end{aligned}
\tag{64}
$$

References

[1] M. Ainsworth, Dispersive and dissipative behaviour of high order discontinuous Galerkin finite element methods, J. Comput. Phys. 198 (2004) 106–130.
[2] J. Berland, C. Bogey, C. Bailly, Low-dissipation and low-dispersion fourth-order Runge–Kutta algorithm, Comput. Fluids 35 (2006) 1459–1463.
[3] J.C. Butcher, The Numerical Analysis of Ordinary Differential Equations, Runge–Kutta and General Linear Methods, Wiley, New York, 1987.
[4] M. Calvo, J.M. Franco, L. Randez, A new minimum storage Runge–Kutta scheme for computational acoustics, J. Comput. Phys. 20 (2004) 11–12.
[5] M. Carpenter, C. Kenney, Fourth-order 2*N*-storage Runge–Kutta schemes, NASA Technical Memorandum 109112, 1994.
[6] B. Cockburn, C.-W. Shu, TVB Runge–Kutta local projection discontinuous Galerkin finite element method for conservation laws. V: Multidimensional systems, J. Comput. Phys. 141 (1998) 199–224.
[7] B. Cockburn, C.-W. Shu, Runge–Kutta discontinuous Galerkin methods for convection dominated problems, J. Sci. Comput. 16 (2001) 173–261.
[8] M. Dumbser, C.-D. Munz, Building blocks for arbitrary high order discontinuous Galerkin schemes, J. Sci. Comput. 27 (2006) 215–230.
[9] M. Dumbser, M. Käser, E.F. Toro, An arbitrary high order discontinuous Galerkin method for elastic waves on unstructured meshes. V: Local time stepping and *p*-adaptivity, Geophys. J. Int. 171 (2007) 695–717.
[10] M. Dumbser, M. Käser, Arbitrary high order non-oscillatory finite volume schemes on unstructured meshes for linear hyperbolic systems, J. Comput. Phys. 221 (2007) 693–723.
[11] M. Dumbser, C.-D. Munz, Arbitrary high-order discontinuous Galerkin schemes, in: S. Cordier, T. Goudon, M. Gutnic, E. Sonnendrunker (Eds.), Numerical Methods for Hyperbolic and Kinetic Problems, EMS Publishing House, 2005, pp. 295–333.
[12] J.E. Flaherty, R.M. Loy, M.S. Shephard, B.K. Szymanski, J.D. Teresco, L.H. Ziantz, Adaptive local refinement with octree load-balancing for the parallel solution of three-dimensional conservation laws, J. Parallel Distrib. Comput. 47 (1997) 139–152.
[13] T.L. Garrec, X. Gloerfelt, C. Corre, Multi-size-mesh, multi-time-step algorithm for noise computation around an airfoil in curvilinear meshes, AIAA Paper 2007-3504, 2007.
[14] G. Gassner, F. Lörcher, C.-D. Munz, A discontinuous Galerkin scheme based on a space-time expansion. I: Inviscid compressible flow in one space dimension, J. Sci. Comput. 32 (2007) 175–199.
[15] G. Gassner, F. Lörcher, C.-D. Munz, A discontinuous Galerkin scheme based on a space–time expansion. II: Viscous flow equation in multi dimensions, J. Sci. Comput. 34 (2008) 260–286.
[16] C. Gear, D. Wells, Multirate linear multistep method, BIT 24 (1984) 484–502.
[17] N. Godel, S. Schomann, T. Warburton, M. Clemens, Local timestepping discontinuous Galerkin methods for electromagnetic RF field problems, in: Antennas and Propagation, EuCAP 2009 Conference, March 2009, pp. 2149–2153.
[18] S. Gottlieb, C.-W. Shu, Total variation diminishing Runge–Kutta schemes, Math. Comput. 67 (1998) 73–85.
[19] M. Gunther, A. Kvarno, P. Rentrop, Multirate partitioned Runge–Kutta methods, BIT 41 (2001) 504–514.
[20] F.Q. Hu, H.L. Atkins, Eigensolution analysis of the discontinuous Galerkin method with nonuniform grids I: One space dimension, J. Comput. Phys. 182 (2002) 516–545.
[21] F.Q. Hu, H.L. Atkins, Two dimensional wave analysis of the discontinuous Galerkin method with nonuniform grids and boundary conditions, AIAA Paper 2002-2514, 2002.
[22] F.Q. Hu, M.Y. Hussaini, J.L. Manthey, Low-dissipation and low-dispersion Runge–Kutta schemes for computational acoustics, J. Comput. Phys. 124 (1996) 177–191.
[23] F.Q. Hu, M.Y. Hussaini, P. Rasetarinera, An analysis of the discontinuous Galerkin method for wave propagation problems, J. Comput. Phys. 151 (1999) 921–946.
[24] F.Q. Hu, A perfectly matched layer absorbing boundary condition for linearized Euler equations with a non-uniform mean flow, J. Comput. Phys. 208 (2004) 469–492.
[25] A. Jameson, W. Schmidt, E. Turkel, Numerical solutions of the Euler equations by the finite volume methods using Runge–Kutta time stepping schemes, AIAA Paper 81-1259, 1981.
[26] C. Johnson, Numerical Solution of Partial Differential Equations by the Finite Element Method, Cambridge University Press, Cambridge, 1987.
[27] C. Johnson, J. Pitkäranta, An analysis of the discontinuous Galerkin method for a scalar hyperbolic equation, Math. Comput. 46 (1986) 1–26.
[28] A. Kanevsky, M.H. Carpenter, D. Gottlieb, J.S. Hesthaven, Application of implicit–explicit high-order Runge–Kutta methods to discontinuous Galerkin schemes, J. Comput. Phys. 225 (2007) 1753–1781.
[29] P. Lesaint, P.-A. Raviart, On a finite element method for solving the neutron transport equation, in: C. de Boor (Ed.), Mathematical Aspects of Finite Elements in Partial Differential Equations, Academic Press, New York, 1974.
[30] D.K. Lin, M. Jiang, X.D. Li, A multi-time-step strategy based on an optimized time interpolation scheme for overset grids, J. Comput. Acoust. 18 (2010) 1–18.
[31] T. Peterson, A note on the convergence of the discontinuous Galerkin method for a scalar hyperbolic equation, SIAM J. Numer. Anal. 28 (1991) 133–140.
[32] J.X. Qiu, M. Dumbser, C.-W. Shu, The discontinuous Galerkin method with Lax–Wendroff type time discretizations, Comput. Methods Appl. Mech. Eng. 194 (2005) 4528–4543.
[33] J.X. Qiu, B.C. Khoo, C.-W. Shu, A numerical study for the performance of the Runge–Kutta discontinuous Galerkin method based on different numerical fluxes, J. Comput. Phys. 212 (2006) 540–565.
[34] W.H. Reed, T.R. Hill, Triangular mesh methods for the neutron transport equation, LA Report, 1973.
[35] V. Savcenco, W. Hundsdorfer, J.G. Verwer, A multirate time stepping strategy for stiff ordinary differential equations, BIT 47 (2007) 137–155.
[36] D. Stanescu, W.G. Habashi, 2*N*-storage low dissipation and dispersion Runge–Kutta schemes for computational acoustics, J. Comput. Phys. 143 (1998) 674–681.
[37] C.K.W. Tam, J.C. Hardin, Second computational aeroacoustics (CAA) workshop on benchmark problems, NASA CP 3352, 1997.
[38] C.K.W. Tam, K.A. Kurbatskii, Multi-size-mesh multi-time-step dispersion-relation-preserving scheme for multiple-scales aeroacoustics problems, Int. J. Comput. Fluid Dynam. 17 (2003) 119–132.
[39] V.A. Titarev, E.F. Toro, ADER schemes for three-dimensional nonlinear hyperbolic systems, J. Comput. Phys. 204 (2005) 715–736.